Journal of Geophysical Research: Space Physics

RESEARCH ARTICLE
10.1029/2017JA024729

Special Section:
Mars Aeronomy

Reconnection in the Martian Magnetotail: Hall-MHD With Embedded Particle-in-Cell Simulations

Yingjuan Ma[1], Christopher T. Russell[1], Gabor Toth[2], Yuxi Chen[2], Andrew F. Nagy[2], Yuki Harada[3], James McFadden[4], Jasper S. Halekas[3], Rob Lillis[4], John E. P. Connerney[5], Jared Espley[5], Gina A. DiBraccio[5], Stefano Markidis[6], Ivy Bo Peng[6], Xiaohua Fang[7], and Bruce M. Jakosky[7]

[1]Department of Earth, Planetary and Space Sciences, University of California, Los Angeles, CA, USA, [2]Department of Climate and Space Sciences and Engineering, University of Michigan, Ann Arbor, MI, USA, [3]Department of Physics and Astronomy, University of Iowa, Iowa City, IA, USA, [4]Space Sciences Laboratory, University of California, Berkeley, CA, USA, [5]NASA Goddard Space Flight Center, Greenbelt, MD, USA, [6]High Performance Computing and Visualization, KTH, Stockholm, Sweden, [7]Laboratory for Atmospheric and Space Physics, University of Colorado Boulder, Boulder, CO, USA

Key Points:
- Model results show that the Martian magnetotail is highly dynamic due to magnetic reconnection
- The numerical simulations predict that the Mars-ward plasma flow, due to magnetic reconnection, is faster for lighter ions, consistent with MAVEN observations
- The HMHD EPIC model simulations predict that the ion loss rates are more variable but with similar mean values as compared with HMHD model

Correspondence to:
Y. Ma,
yingjuan@igpp.ucla.edu

Citation:
Ma, Y., Russell, C. T., Toth, G., Chen, Y., Nagy, A. F., Harada, Y., et al. (2018). Reconnection in the Martian magnetotail: Hall-MHD with embedded particle-in-cell simulations. *Journal of Geophysical Research: Space Physics*, *123*, 3742–3763. https://doi.org/10.1029/2017JA024729

Received 31 AUG 2017
Accepted 20 APR 2018
Accepted article online 30 APR 2018
Published online 18 MAY 2018

Abstract Mars Atmosphere and Volatile EvolutioN (MAVEN) mission observations show clear evidence of the occurrence of the magnetic reconnection process in the Martian plasma tail. In this study, we use sophisticated numerical models to help us understand the effects of magnetic reconnection in the plasma tail. The numerical models used in this study are (a) a multispecies global Hall-magnetohydrodynamic (HMHD) model and (b) a global HMHD model two-way coupled to an embedded fully kinetic particle-in-cell code. Comparison with MAVEN observations clearly shows that the general interaction pattern is well reproduced by the global HMHD model. The coupled model takes advantage of both the efficiency of the MHD model and the ability to incorporate kinetic processes of the particle-in-cell model, making it feasible to conduct kinetic simulations for Mars under realistic solar wind conditions for the first time. Results from the coupled model show that the Martian magnetotail is highly dynamic due to magnetic reconnection, and the resulting Mars-ward plasma flow velocities are significantly higher for the lighter ion fluid, which are quantitatively consistent with MAVEN observations. The HMHD with Embedded Particle-in-Cell model predicts that the ion loss rates are more variable but with similar mean values as compared with HMHD model results.

1. Introduction

Magnetic reconnection is a fundamental physical process in space plasmas in which the magnetic topology changes rapidly and magnetic energy is converted to kinetic energy through acceleration or heating of charged particles (Burch et al., 2016; Paschmann et al., 2013; Sonnerup, 1979). The magnetic reconnection process plays important roles in many space plasma environments, producing various phenomena such as solar flares, coronal mass ejections, geomagnetic storms, and cometary tail disconnection (Angelopoulos et al., 2008; Lin & Forbes, 2000; Masuda et al., 1994; Russell et al., 1986; Yokoyama et al., 2001).

Magnetic reconnection is a cross-scale phenomenon (Paschmann et al., 2013). The magnetic reconnection region contains three distinct layers: the large-scale outer layer, where the fluid approximation and frozen-in conditions are appropriate; a small-scale ion diffusion region; and a microscale electron diffusion region in the close vicinity of the reconnection X line. The thickness of the ion diffusion region is a few ion inertial lengths (c/ω_{pi}, where c is the speed of light and ω_{pi} is the ion plasma frequency). In this region, ions are demagnetized and decoupled from the electrons; thus non-MHD effects are important. Kinetic simulations (Hesse et al., 2001) and observations (Øieroset et al., 2001) showed that Hall currents are generated inside the region associated with the formation of the out-of-plane quadrupolar magnetic fields. The electron diffusion region is about 43 times (the square root of the proton-electron mass ratio) smaller than the ion diffusion region. Magnetic reconnection is initiated inside the electron diffusion region, where electrons are demagnetized. In this region, electron inertial and nonisotropic pressure gradient effects become important to produce a parallel electric field and current, which together cause the dissipation of magnetic energy (Paschmann et al., 2013; Yamada et al., 2010).

At magnetized planets with global dynamo fields, such as Earth, magnetic reconnection between solar and planetary magnetic fields plays a central role in the dynamics of the intrinsic magnetospheres (e.g.,

Dungey, 1961; Russell, 2001; Southwood & Chané, 2016). When the direction of the interplanetary magnetic field is opposite to the planetary magnetic field, magnetic reconnection has been observed both on the dayside magnetopause (Paschmann et al., 1979; Phan et al., 2000) and in the magnetotail (Øieroset et al., 2001). This process allows mass and momentum transfer from the solar wind into the magnetosphere (Mozer et al., 2002).

Magnetic reconnection was also observed at unmagnetized planets such as Venus and Mars (Eastwood et al., 2008; Halekas et al., 2009; Zhang et al., 2012), but the role of magnetic reconnection is still poorly understood because of the scarcity of relevant in situ observations. Plasma environments around Venus and Mars are drastically different compared with that of the Earth, due to the lack of substantial planetary magnetic fields (Nagy et al., 2004; Russell et al., 2006, 2007). As there are no strong internal magnetic fields to stand off the fast-flowing solar wind, unmagnetized planets interact with the solar wind in a much more direct way, with the highly conducting planetary ionosphere as the primary obstacle to the flow. The solar wind is heated and slowed across the shock and diverted around in the magnetosheath region. Inside the sheath is a well-defined thin plasma boundary named the magnetic pileup boundary (MPB), which separates the magnetic pileup region from the shocked solar wind. The magnetic field piles up and drapes around the highly conducting dayside ionosphere. The draping fields form a magnetotail on the nightside with antiparallel magnetic fields in the two lobes, with the polarity of the field controlled by the orientation of the transverse (relative to the flow) component of the interplanetary magnetic field (Schwingenschuh et al., 1992; Yeroshenko et al., 1990).

The first direct evidence of collisionless magnetic reconnection at Mars was reported by Eastwood et al. (2008), using data from Mars Global Surveyor (MGS), in combination with particle-in-cell (PIC) simulations of reconnection. The evidence (including the Hall magnetic field structure, bifurcated current sheets (CSs), wave activity, and secondary islands) indicated that the spacecraft passed through the diffusion region where reconnection was initiated. Halekas et al. (2009) surveyed all the MGS mapping data and found 26 reconnection events, mostly in the tail region or terminator/polar regions, with magnetic fields consistent with the expected polarities of Hall fields near the diffusion regions. However, MGS did not carry any ion instruments onboard, thus no simultaneous ion measurements were available associated with those magnetic reconnection events precluding the evaluation of the reconnection effect on ions.

A magnetic reconnection event was recently reported based on plasma observations from the ongoing Mars Atmosphere and Volatile EvolutioN (MAVEN) mission (Jakosky et al., 2015). The MAVEN payload conducts simultaneous measurements of ions, electrons, and magnetic fields with the state-of-the-art instruments with sufficient time, energy, angle, and mass resolution, thus for the first time providing comprehensive demonstration of magnetic reconnection signatures in the Martian magnetotail (Harada et al., 2015). The first MAVEN reconnection event was observed on 4 December 2014, a month after the spacecraft began science operations. The observed reconnection signatures include the closed magnetic field topology in the central tail CS, Hall magnetic fields, Mars-ward ion bulk flows with counterstreaming beams in the closed-field region, the coexistence of cold ion inflow and Mars-ward O_2^+ ion beams with energy dispersion in the separatrix region (Harada et al., 2015). Given the ever-changing magnetic topology and the complex interplay between solar wind, crustal, and draped magnetospheric field lines at Mars, it was suspected that reconnection should be relatively common in the Martian magnetosphere (Halekas et al., 2009). Recently, Harada et al. (2017) conducted an extended survey of reconnection signatures observed in the Martian magnetotail by the MAVEN mission and estimated that the occurrence rate of tail reconnection is ~1–10% or even higher. Some studies suggested that reconnection may play a crucial role in controlling the dynamics of the Martian magnetotail (Brain, 2006; Brain et al., 2010; Halekas et al., 2011; Krymskii et al., 2002).

As the magnetotail provides one of the major channels through which planetary ions escape from unmagnetized planets (Barabash, Fedorov, Lundin, et al., 2007; Barabash, Fedorov, Sauvaud, et al., 2007; Brain et al., 2010; Dubinin et al., 2011), understanding the magnetic reconnection process and associated particle acceleration mechanism in the magnetotail is a critical step toward determining the atmospheric loss of unmagnetized planets. In this paper, we focus on the 4 December 2014 magnetic reconnection event observed by MAVEN, studying numerically the magnetic reconnection process and its global consequences in the plasma tails of Mars. The description of the numerical models and detailed coupling algorithm are provided in section 2. The simulation setup and model results are presented for the Hall-MHD (HMHD) model in

section 3, together with the comparison of model results with relevant MAVEN plasma observations along the spacecraft orbit for the magnetic reconnection event. Results from the HMHD with Embebded Particle-in-Cell (EPIC) model are presented in section 4. The paper is concluded with a brief summary in section 5.

2. Methodology

We use both a global HMHD model and an innovative two-way coupled fluid-kinetic approach to study the effect of the magnetic reconnection process at Mars. The HMHD model has been applied to Titan (Ma et al., 2007). The two-way coupled model links the global HMHD model with an embedded PIC code. Such modeling capability has been developed recently (Daldorff et al., 2014) in the SWMF (Space Weather Modeling Framework) at the University of Michigan to couple the MHD model with a 3-D semi-implicit PIC (iPIC3D) model (Markidis et al., 2010). It has been successfully applied to Ganymede (Tóth et al., 2016) and Earth (Chen et al., 2017), and this approach is adapted to Mars in this study. The MHD EPIC algorithm takes advantage of the efficiency of the global MHD model and the ability of the PIC model to include kinetic effects. This makes it feasible to perform kinetic simulations of reconnection under realistic solar wind condition.

2.1. Multispecies HMHD Model of Mars

The global MHD model for Mars uses the state-of-the-art BATS-R-US (Block Adaptive-Tree Solar-wind Roe-type Upwind Scheme) platform (Powell et al., 1999; Tóth et al., 2012). The BATS-R-US code uses a block-based grid structure, which allows refining the grid in the selected regions of interest to achieve high resolution and coarsen the grid in less-interesting regions to lower resolution.

The multispecies MHD model of Mars has been described in detail by Ma et al. (2004); Ma et al. (2014). The model self-consistently calculates the magnetic field, plasma velocity, and mass densities of protons and three major ionospheric ion species (O^+, O_2^+, and CO_2^+). A 3-D realistic ionosphere is generated self-consistently in the model by considering major ionization sources, including photoionization and electron impact ionization together with density changes caused by charge exchange and dissociative recombination reactions.

The multispecies MHD model of Mars has been recently upgraded to include the rotation of the crustal field (Ma et al., 2014) in a time-dependent mode and to calculate photoionization rates using an improved method of the Chapman function (Ma et al., 2015) instead of a simple cosine approximation of the solar zenith angle.

In the present study, the Hall term is included in the magnetic induction equation:

$$\frac{\partial \boldsymbol{B}}{\partial t} = \nabla \times \left(\mathbf{u} \times \mathbf{B} - \frac{1}{ne} \mathbf{J} \times \boldsymbol{B} + \frac{1}{ne} \nabla \boldsymbol{P_e} \right) \tag{1}$$

where n is the total ion number density, u is the velocity of ions, e is the unit charge, and P_e is the electron pressure, assumed to be half of the plasma pressure. All the other variables have their conventional meanings. The three terms on the right-hand side of the equation are the convection term, the Hall term, and electron pressure gradient term, respectively. The inclusion of the Hall term allows the ions and electrons to decouple below the ion inertial scale length. The magnetic field lines are still frozen to the electrons, but the "frozen-in" condition between ions and magnetic field lines is broken. The HMHD model has been used in Titan (Ma et al., 2007) and Ganymede (Tóth et al., 2016) simulations. As discussed before, the Hall effect becomes important in the ion diffusion region, so even though the HMHD model is still limited by its fluid assumption, it is more appropriate for the magnetic reconnection study than the MHD model that neglects such an effect. In addition, the coupling of HMHD with PIC model works better than with ideal MHD, because whistler waves can propagate across the interface.

2.1.1. Grid System

Similar to previous Mars model runs (Ma et al., 2014), the calculations are performed in the Mars-centered Solar Orbital coordinate system, with the X axis pointing from Mars to the Sun, the Y axis approximately anti-parallel to Mars' orbital velocity, and the Z axis completing the right-handed coordinate system. The computational domain is set to be $-24R_M < X < 8R_M$, $-16R_M < Y, Z < 16R_M$, where R_M is the radius of Mars

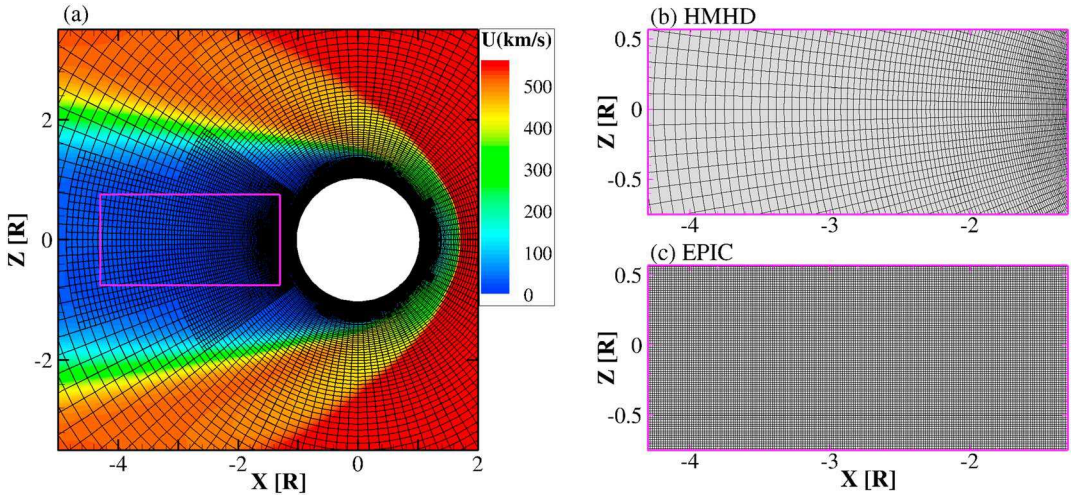

Figure 1. (a) Two-dimensional meridian plane cut of the spherical grid used in the global HMHD model. The purple box shows the region solved by the EPIC code. (b) Zoom in view of the grid inside the purple box for the global MHD model. (c) Grid used in the EPIC model inside the EPIC domain. EPIC = Embeded Particle-in-Cell; HMHD = Hall-magnetohydrodynamic.

(R_M = 3,396 km). This computational domain is large enough to minimize numerical artifacts from the outer boundary.

Figure 1 shows the 2-D meridian plane cut of the grid used in the global model. We use a nonuniform spherical grid to provide high radial resolution in the ionosphere (~10 km). The angular resolution is 3° uniformly in both azimuthal and longitudinal direction. The grid is similar to previous Mars runs (Ma et al., 2014), except an additional refinement is performed in the tail region to provide better resolution near the reconnection site. The grid resolution in radial direction varies from 30 km in radial direction at $-1.3R_M$ to 270 km at $-4.5R_M$. The total number of cells used in the simulation is roughly 1.3 million.

2.1.2. Boundary Conditions

The inner boundary conditions are the same as used in Ma et al. (2004); Ma et al. (2014); and Ma et al. (2015). The inner boundary is set at 100-km altitude, which is a collision-dominated region. Since the ion transport is negligibly small in such regions, it is safe to assume that all the ion densities are in photochemical equilibrium at the inner boundary. Plasma temperature (T_P) is assumed to be twice the neutral temperature, and the pressure is set accordingly at the inner boundary. The magnetic field is set to be the same as the crustal magnetic field. Note that the crustal field model is updated with a degree and order 110 spherical harmonic model (Morschhauser et al., 2014). Comparison of this model and the Arkani-Hamed (2001, 2002) order 60 model shows a small difference in the strong crustal field region but a relatively large difference in the weak crustal field regions. The new crustal field model has lower noise, especially in the weak crustal field regions. The crustal field configuration is updated every 10 s using the actual rotation axis and rotation period.

2.2. Implicit PIC Model: iPIC3D

As non-MHD effects play important roles in the magnetic reconnection process, a kinetic model is needed to numerically study the reconnection process. The most frequently used kinetic approach is the PIC model, which solves for the motion of electron and ion macroparticles (computational particles that represent many real particles), together with the full set of Maxwell's equations for the electric and magnetic fields. In this study, the implicit PIC code iPIC3D (Markidis et al., 2010) is applied to the plasma tail region to understand the magnetic reconnection process. This model solves the electromagnetic fields on a uniform 3-D Cartesian grid with an implicit scheme, which can eliminate the severe numerical stability constraints of the explicit PIC algorithm. It allows a large simulation time step (hundreds of times the electron plasma frequency), reaching MHD timescales but still retaining plasma kinetic effects.

In the iPIC3D model, particles are initialized with a specific number of ion and electron macroparticles per grid cell. The particles can freely move between the cells based on the Lorentz force. A coupled boundary

is used for the PIC model to mimic the inflow and outflow of the plasma into/out from the simulation domain (Chen et al., 2017; Peng et al., 2015). A particle is simply lost if it exits the boundary of the PIC domain. Particles can also move into the PIC region from the surrounding ghost cells, which are filled in with N_i ion macroparticles for each ion species and N_e electron macroparticles for every time step based on boundary conditions provided by the HMHD model. The total number of particles in each cell can change in the simulation but normally does not differ significantly from the original number. The mass ratio of proton to electron is set to $M_p/M_e = 100$, which is smaller than the real ratio. Studies have shown that the timescale of magnetic reconnection onset is nearly independent of the electron mass. The implicit PIC algorithm has been validated for both the antiparallel and the guide field reconnection cases and demonstrated both the effectiveness of algorithm and the ability of the code to solve multiscale problems (Markidis et al., 2011, 2013).

2.3. MHD EPIC Coupling Within the Space Weather Modeling Framework

The BATS-R-US and iPIC3D models have been integrated into and coupled through the SWMF. Details of the coupling approach between the BATS-R-US and iPIC3D models have been provided in Daldorff et al. (2014). The coupled model has been successfully applied to Ganymede (Tóth et al., 2016) and Earth (Chen et al., 2017).

To study the reconnection event at Mars, we first obtain an approximate steady state solution by running the multispecies global HMHD model of Mars in time-dependent mode for sufficient long time (1-hr physical time in this case) in the full computational domain. Based on the global HMHD model results, the potential reconnection regions can be identified based on magnetic field geometry. Then, we restart the SWMF in the coupling mode with the PIC domain specified around the reconnection sites. At the beginning of the first time step of the coupling, the MHD solution (density of each ion species, velocity and temperature, and magnetic field) inside and around the PIC regions is sent to iPIC3D, which initializes the ion and electron macroparticles assuming Maxwellian distributions with the same mass, momentum, and energy densities as the MHD solution, with the algorithm detailed by Daldorff et al. (2014). Different ion macroparticles have different weights based on their mass densities but are initialized with the same bulk velocity and temperature. MHD model passes the magnetic field B to PIC, and the electric field is calculated as $E = -u_e \times B$, with the Hall effect included. Here u_e is electron velocity, which is defined as $u_e = u_i - J/ne$. In subsequent time steps, the iPIC3D is advanced with boundary conditions provided by BATS-R-US, which is used to generate particles and to set the magnetic and electric fields in the ghost cells of the PIC grid. The iPIC3D solution is then sent back to BATS-R-US to overwrite the MHD results inside the PIC domain. Note that the electron pressure gradient term is currently neglected when the electric field is initialized for the PIC code from the MHD solution, and similarly, it is neglected when the electric field is calculated from the MHD quantities at the boundaries of the PIC domain. This term is typically quite small away from the reconnection site, so its effect on the plasma dynamics should be negligible. Once the PIC model has run for a while, the effects of the initial conditions are erased, while the boundaries of the PIC domain are typically placed far from the reconnection sites. In fact, we checked and found that at the boundaries of the PIC region, the electron pressure gradient force is about 2 orders smaller than the electromagnetic force and thus can be safely neglected. In the near future, we do plan to implement the gradient P_e term in the coupling for sake of completeness, but we do not expect that this would have a significant effect on the solution.

To make the MHD EPIC applications more productive, a new general coupler has been developed to efficiently transfer data between the BATS-R-US and iPIC3D processes (Tóth et al., 2016). The new coupler can be applied to arbitrary grids, and it allows the BATS-R-US and iPIC3D to use different grid structure, grid resolution, and time step. This is particularly important for the application to Mars, as the global MHD model of Mars is using an adaptive spherical grid structure. This is also the first time that the PIC model is coupled with a multispecies global MHD model. As there are multiple ions coexisting in the Martian tail, this feature is essential in order to properly simulate the reconnection process at Mars. Multi-ion reconnection has been investigated using two and half dimensional PIC simulations with two ion species included (Liu et al., 2015; Markidis et al., 2011). Both found that presence of the heavy ions could slow down the magnetic reconnection rate.

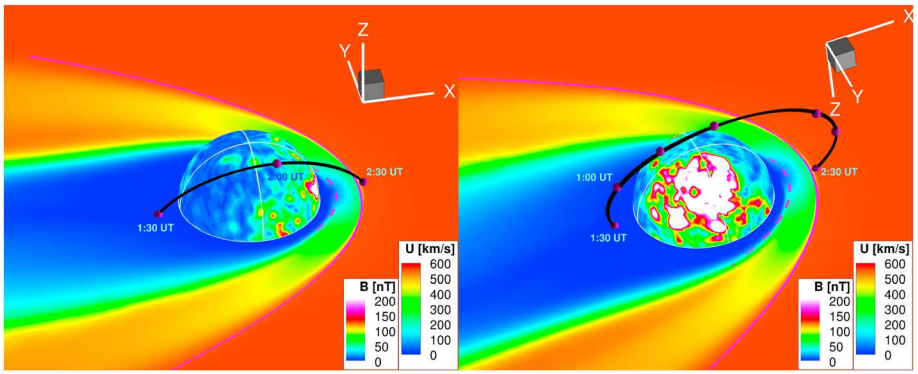

Figure 2. Three-dimensional view of Mars Atmosphere and Volatile EvolutioN trajectory (black curve) from 0 UT to 4 UT on 4 December 2014, from two different viewing angles. Left (right) panel corresponds to downward view of the Northern (Southern) Hemisphere. The color on the sphere corresponds to the crustal field magnitude at 1:30 UT on 4 December. The color in the ecliptic plane shows the flow speed from the Hall-magnetohydrodynamic model. The observed bow shock and magnetic pileup boundary boundaries from Vignes et al. (2000) are plotted in solid and dashed purple lines as references.

3. Results From the HMHD Model of Mars

3.1. MAVEN Orbit and Model Setup

MAVEN's trajectory during the 4 December 2014 magnetic reconnection event is shown by the black curve in Figure 2. It is plotted in the context of the global MHD model results to give a rough idea about the different plasma regions that MAVEN was passing through. The spacecraft was moving from the Southern Hemisphere to the Northern Hemisphere. It was passing through the central plasma sheet when several reconnection signatures were observed around 1:30 UT.

Table 1 lists solar wind conditions right before inbound bow shock crossings (00:04 UT) and shortly after the outbound crossings (02:37 UT). There are some variations in the solar wind density, velocity, and magnetic field strength from inbound to outbound. The magnetic field direction altered significantly, from positive Z to a positive Y dominant field, rotated ~136°. MAVEN passed periapsis (~164-km altitude) around 1:50 UT, which was on the nightside and close to the terminator.

The photoionization rates are based on extreme ultraviolet observations from the extreme ultraviolet monitor (Eparvier et al., 2015), and the ionization rates were 8.02×10^{-7} for CO_2 and 2.54×10^{-7} for O, for the day. These ionization rates are slightly higher than the values used for typical solar maximum conditions (Schunk & Nagy, 2009). To be consistent, the neutral profiles used here are also for solar maximum conditions. Also note that at 1:30 UT, the subsolar point is at 73.1° east longitude and −22.8° latitude, so the strong crustal field region was located in the dusk-midnight sector. The rotational axis was (−0.388, −0.175, 0.905) in the Mars-centered Solar Orbital coordinate. The rotation period was set to 24.67 hr according to the SPICE kernel. During this orbit, the Sun-Mars distance was around 1.38 AU and the Mars season was near southern summer (Ls = 246).

We ran the multispecies HMHD model for 3 hr in a time-dependent mode starting from 2014/12/04-00:00 UT. The inbound solar wind conditions observed by MAVEN as listed in Table 1 are used in the calculation to match with the magnetic field orientation in the CS. The model results are discussed in the following section.

Table 1
Solar Wind Conditions Observed by MAVEN during the 4 December 2014 Reconnection Event

	Time	N_{SW} (cm^{-3})	U_{SW} (km/s)	B_{IMF} (nT)	T_i (K)	T_e (K)
Inbound	00:04 UT	3.9	558	(0.7, −0.4, 2.8) |B| = 2.9	2.2×10^5[a]	1.1×10^5
Outbound	02:37 UT	4.3	577	(0.6, 2.0, −1.6) |B| = 2.6	2.5×10^5[a]	1.1×10^5

[a]The temperatures used here are from Mars Atmosphere and Volatile EvolutioN (MAVEN) in situ key parameter data set. The actual ion temperature using a detailed analysis when removing the effect from alpha particles is ~30% lower than listed.

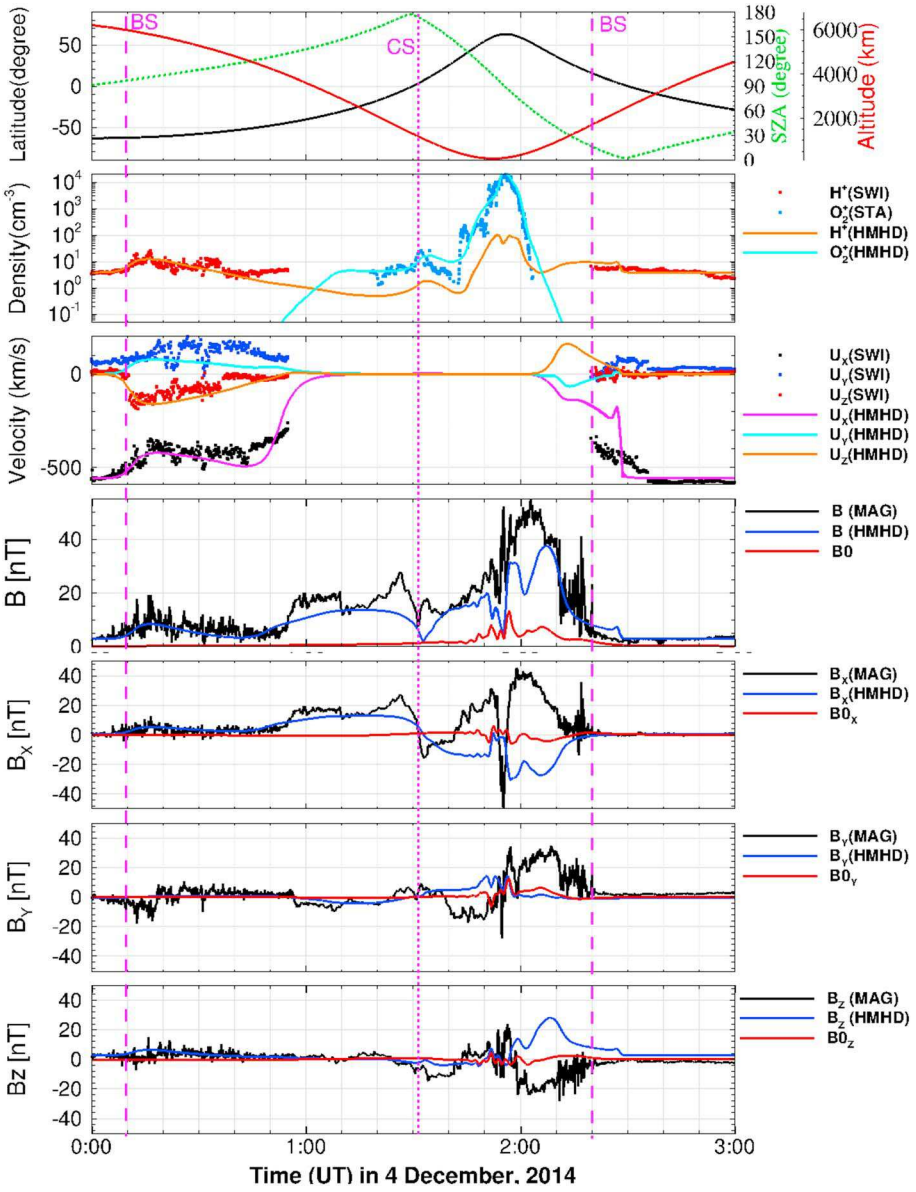

Figure 3. Comparison of Hall-magnetohydrodynamic (HMHD) model results and MAVEN observations along the orbit. Top panel shows the satellite latitude, solar zenith angle, and altitude along the trajectory. Second to seventh panels show comparison of the plasma density, velocity, and magnetic field with relevant plasma observations along the MAVEN orbit. The vertical lines mark the locations of different plasma boundaries that MAVEN passed: Bow shock (dashed lines) and current sheet (dotted line). MAVEN = Mars Atmosphere and Volatile EvolutioN.

3.2. Comparison of HMHD Results With MAVEN Observations

The time-dependent HMHD simulation enables a direct comparison of the model prediction with MAVEN observations along the spacecraft orbit as shown in Figure 3. Model results of the plasma properties (density and velocity vector) and magnetic field and the comparison with relevant plasma observations are all presented in the figure. The top panel shows the satellite latitude, solar zenith angle, and altitude along the trajectory. Comparison of plasma density is shown in the second panel. HMHD model predicts that the plasma is dominated by H^+ in the solar wind and sheath region consistent with SWIA (Solar Wind Ion Analyzer; Halekas et al., 2015) observations. In the ionosphere, the dominant ion is O_2^+ as shown by the SupraThermal And Thermal Ion Composition (STATIC; McFadden et al., 2015) observations. Note that Neutral Gas and Ion Mass Spectrometer, which alternates between measuring neutrals and ions every other orbit, was in the neutral mode during this orbit. Overall, both the plasma density and composition are well

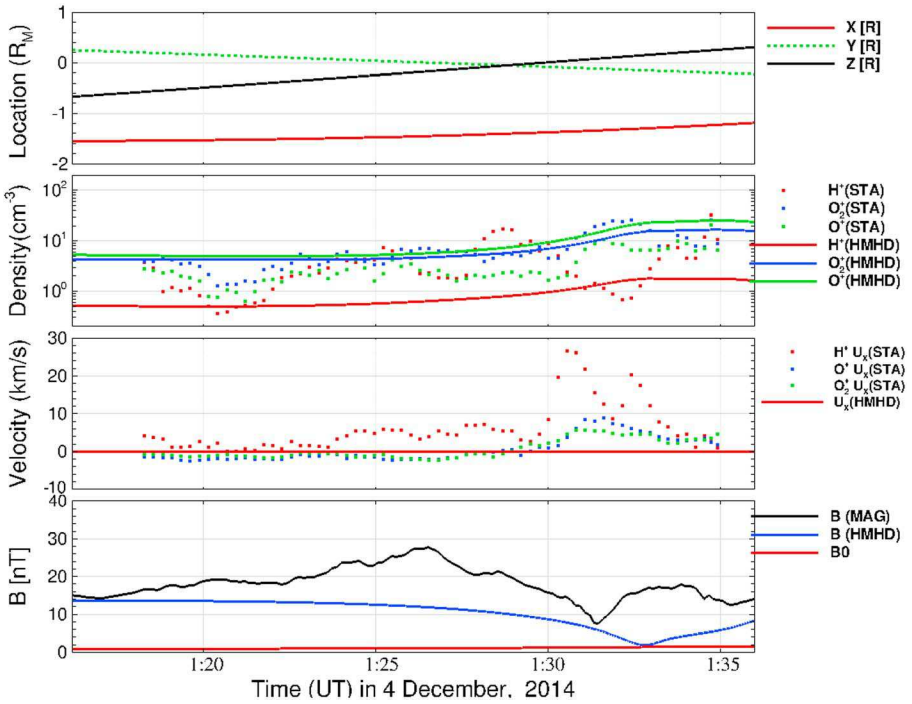

Figure 4. Comparison of Hall-magnetohydrodynamic (HMHD) model results and MAVEN observations in the Martian magnetotail. The top panel shows the satellite position. Second to fourth panels show comparison of the plasma density, velocity, and magnetic field strength with relevant plasma observations along the MAVEN orbit. MAVEN = Mars Atmosphere and Volatile EvolutioN.

reproduced by the model along most of the orbit, except in the tail region. The density from the model is rather smooth, while the observations suggest the existence of small structures in the tail region, which are not reproduced by the fluid model.

Comparison of plasma velocity is shown in the third panel. Outside of the inbound bow shock crossing, plasma was mainly moving antisunward with a small positive U_Y component as shown by SWIA observations, consistent with the expected aberration due to the orbital velocity of Mars around the Sun. Inside the sheath region, the plasma flow was gradually slowed down and diverted, with a significant negative U_Z component, as the S/C was passing the sheath region in the Southern Hemisphere. The plasma flow velocity as predicted by the model matches well with SWIA observations.

Comparison with field strength and components measured by the magnetometer (Connerney et al., 2015) are shown in the rest of the panels, together with crustal magnetic field calculated from the Morschhauser et al. (2014) model. The crustal magnetic field is rather weak during the orbit, with a peak field strength of 12 nT near periapsis. The magnetic field was nearly 3 nT in the solar wind and was enhanced to 10 nT across the shock. The magnetic field strength reached a local minimum around 1:30 UT, in the CS, as the B_X component changing from positive to negative values across the CS. The CS corresponds to low magnetic field but high-density plasma. The model predicts that the time of the CS crossing is 1.5 min later than the observation. This may be due to uncertainty in the solar wind condition. Both magnetic field strength and direction during the outbound part of the orbit shortly after the crossing of the CS were not very well reproduced by the model due to the IMF direction change as listed in Table 1.

We also conducted a similar calculation using outbound solar wind conditions and found a better match for the outbound part of the trajectory, as expected. The field orientation around the CS suggests that the solar wind conditions had changed most likely after the CS crossing, so we use the inbound solar wind condition as input to drive the coupled HMHD EPIC model, as will be discussed in more detail in the next section.

Figure 4 shows data-model comparison along the MAVEN orbit zoomed in the Martian magnetotail. As can be seen from the second panel, the plasma is composed mainly by two planetary ions (O^+ and O_2^+) as observed by STATIC. The densities of O^+ and O_2^+ from the HMHD model are about the same level as the

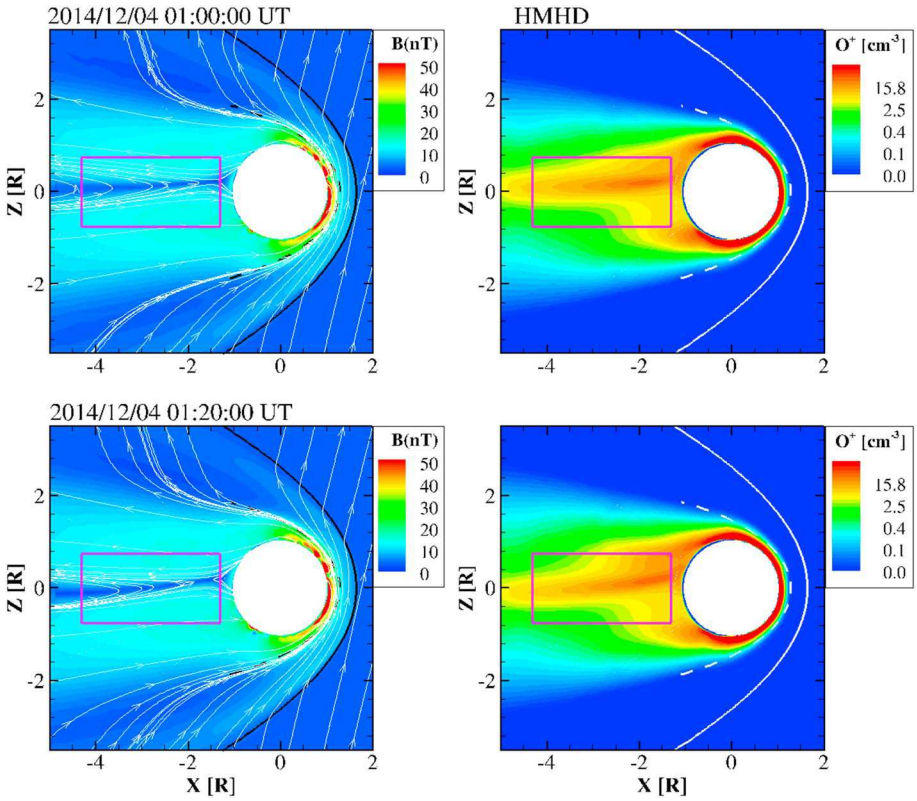

Figure 5. Two snapshots of the contour plots of magnetic field and O^+ density in the *XZ* plane from the time-dependent Hall-magnetohydrodynamic (HMHD) simulation. The left panels show contour plots of magnetic strength together with magnetic field lines (white lines), and the right panels show contours of O^+ density. The purple rectangle shows the embedded particle-in-cell region as references. The observed bow shock and magnetic pileup boundary boundaries from Vignes et al. (2000) are plotted in solid and dashed lines.

observations but lacking the small structures. Model predicts a somewhat lower proton density compared with STATIC, indicating that the concentration of proton in the tail region is underestimated by the model. This could be due to the reduced ion chemistry used in the model, which works well for dayside ionosphere but may be oversimplified for the nightside ionosphere. The third panel shows velocity comparison along the MAVEN orbit. The single-fluid assumption of the HMHD model could not reproduce the velocity difference observed for different ion species. The bottom panel of Figure 4 shows a comparison of the modeled and observed magnetic field strengths together with crustal magnetic field (B_0). The crustal field is negligibly small when the magnetic reconnection was observed. The magnetic field strength from the model follows roughly the same trend as the observation, but the strength from the model is significantly smaller than the value observed by the S/C.

Figure 5 shows two snapshots of the magnetic field and density contour of O^+, from the time-dependent HMHD model corresponding to 01:00 UT and 01:20 UT. For each time, the panel on the left shows magnetic field strength (in color) with magnetic field lines (white lines), and the panel on the right is the density contour of O^+ ions. Similar to the previous numerical and observational studies, we found enhancement of the draping of the magnetic field lines in the magnetic pileup region. As the main component of the upstream magnetic field was in the *Z* direction, the tail CS is located near the equatorial plane. The shock locations and MPB locations from the model results are similar to the mean value derived from past observations (Vignes et al., 2000). O^+ density in the CS is significantly higher than the ambient lobe region. The density distribution in the tail region close to Mars is highly asymmetric in the north-south direction. This is caused by the nonuniform distribution of the crustal field as illustrated in Figure 2. In the Southern Hemisphere, the strong crustal field prohibits the transport of the plasma, resulting in a relative weak plasma density. Comparison of results at the two different times clearly show that according to HMHD model the tail configuration is fairly steady and only slowly varying.

4. Results From the Coupled HMHD EPIC Model

4.1. PIC Region

Based on the HMHD model results, we select the PIC region as $-4.3R_M < X < -1.3R_M$, $-0.75R_M < Y$, $Z < +0.75R_M$, which covers the tail reconnection region of Mars, as shown by the purple box in Figure 1a. Figures 1b and 1c show the grids used in the tail region for the global MHD simulations and the EPIC simulations, respectively.

In the Martian plasma tail, the local CS width is around 520 km, estimated based on the distance along the CS normal traveled by the MAVEN spacecraft (Harada et al., 2015). The ion inertial lengths are ~174 km for H^+, ~363 km for O^+, and ~314 km for O_2^+, based on the average measured ion densities in the closed-field region. To resolve the ion diffusion region, the grid resolution in the PIC domain is taken as $\Delta x = 1/64R_M$ (~50 km), as shown in Figure 1c. Note that the grid resolution in the EPIC simulations is significantly high as compared with the grids used in the global MHD simulations in the same region (see Figure 1b). The PIC domain consists of approximately 1.77 million cells, which are initially filled with 125 ion macroparticles for each of the four ion species and 500 electron macroparticles per cell, resulting in about 1.8 billion particles in total. The relative mass ratios of different ions are set based on the physical mass ratios (16 for O^+, 32 for O_2^+, and 44 for CO_2^+). The HMHD PIC model starts from 01:00 UT, 30 min earlier than the time when the magnetic reconnection was detected. We run the simulation on 1,024 processors for 240 hr on NASA pleaides supercomputer to model 20 min in real time. In terms of computational cost, compared with the time-dependent ideal MHD model, a typical run using the HMHD model requires 3 times more CPU hours, and HMHD EPIC requires 120 times more.

4.2. HMHD EPIC Model Results

Figure 6 shows snapshots of the magnetic field and density contour of O^+, corresponding to $t = 5$, 10, 16, and 18 min after the coupling. The HMHD EPIC model predicts that the region solved by PIC is highly dynamic driven by kinetic processes that are properly captured by the model. The reconnection site varies significantly with time, ranging from $-1.40R_M$ to $-2.0R_M$. Multiple secondary islands can form tail-ward of the reconnection X line and propagating away from the planet as shown at 01:16 UT. Two minutes after, the island that is further away from the planet was moving outside of the PIC domain, with only one magnetic island left. Previous studies show that secondary islands or flux ropes can form when using open boundary conditions due to magnetic reconnection for both antiparallel and component merging scenarios (Daughton et al., 2006). Karimabadi et al. (2011) also demonstrated that the secondary islands form in the presence of O^+ ions, which is consistent with the results from our HMHD EPIC model. The density distribution also varies dramatically with time, with small plasmoids forming and propagating away with the magnetic islands. Also note that there is no noticeable change in the region outside the PIC domain, indicating that the selected PIC region is large enough to contain the regions that are dominated by kinetic processes. The model results clearly show that plasma in the central CS reconnects with magnetic islands forming tail-ward of the reconnection site and propagating away from the planet together with planetary ions. The results shown here are different as compared with Figure 5, in which the dynamic features of the tail region (including the formation and propagation of the plasmoids) are missing from the global HMHD simulations. This is likely due to the fact that the grid resolution used in the global HMHD simulations is much coarser than the grids in the EPIC simulations in the tail region and thus the global HMHD results are affected by the large numerical resistivity (diffusion). As demonstrated by Raeder (2006) and Kuznetsova et al. (2004, 2009), the flux transfer events development depends on sufficient model resolution and on sufficiently low numerical dissipation, flux transfer events do not develop in the model if the numerical resolution is too coarse, which would lead to too much numerical diffusion. However, even if we increase the grid resolution in the global HMHD model to a similar level as that used in the PIC model, many key features, such as different responses of different ion species, electron, and ion phase space distributions, as will be discussed later, cannot be reproduced in the HMHD model. This is because the magnetic reconnection process in the HMHD model relies on numerical resistivity or artificial resistivity, which is not physical. In contrast, the reconnection and flux rope generation mechanism in HMHD EPIC is better represented with proper physics included.

Figure 7 shows the magnetic field (top panels) and the X component of the flow velocities for different ion species as calculated by the PIC model at two different times. The left panels corresponding to simulation

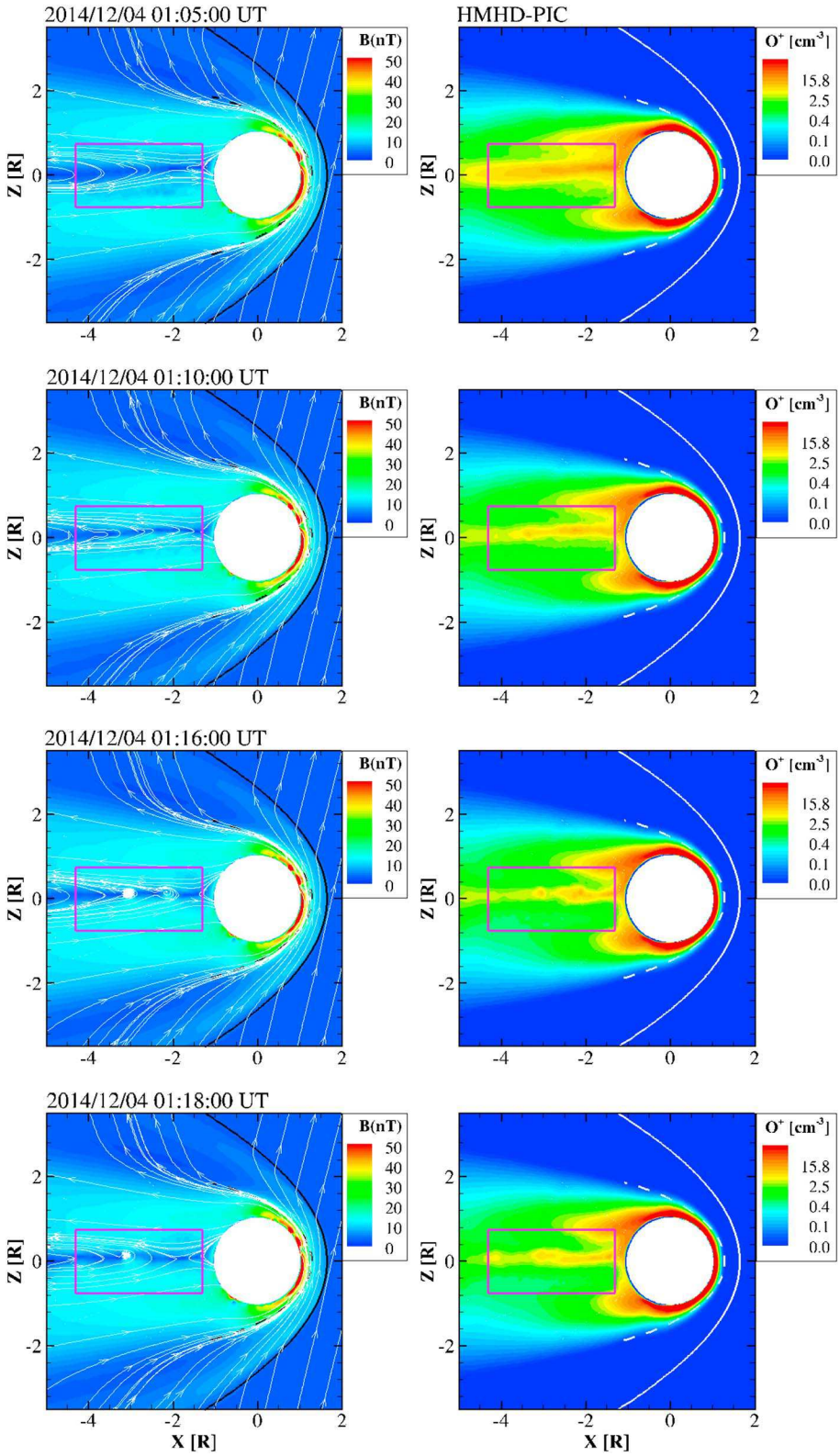

Figure 6. Snapshots of the magnetic field and O^+ density for the Hall-magnetohydrodynamic with embeded Particle-in-Cell run. Figure format is the same as Figure 5.

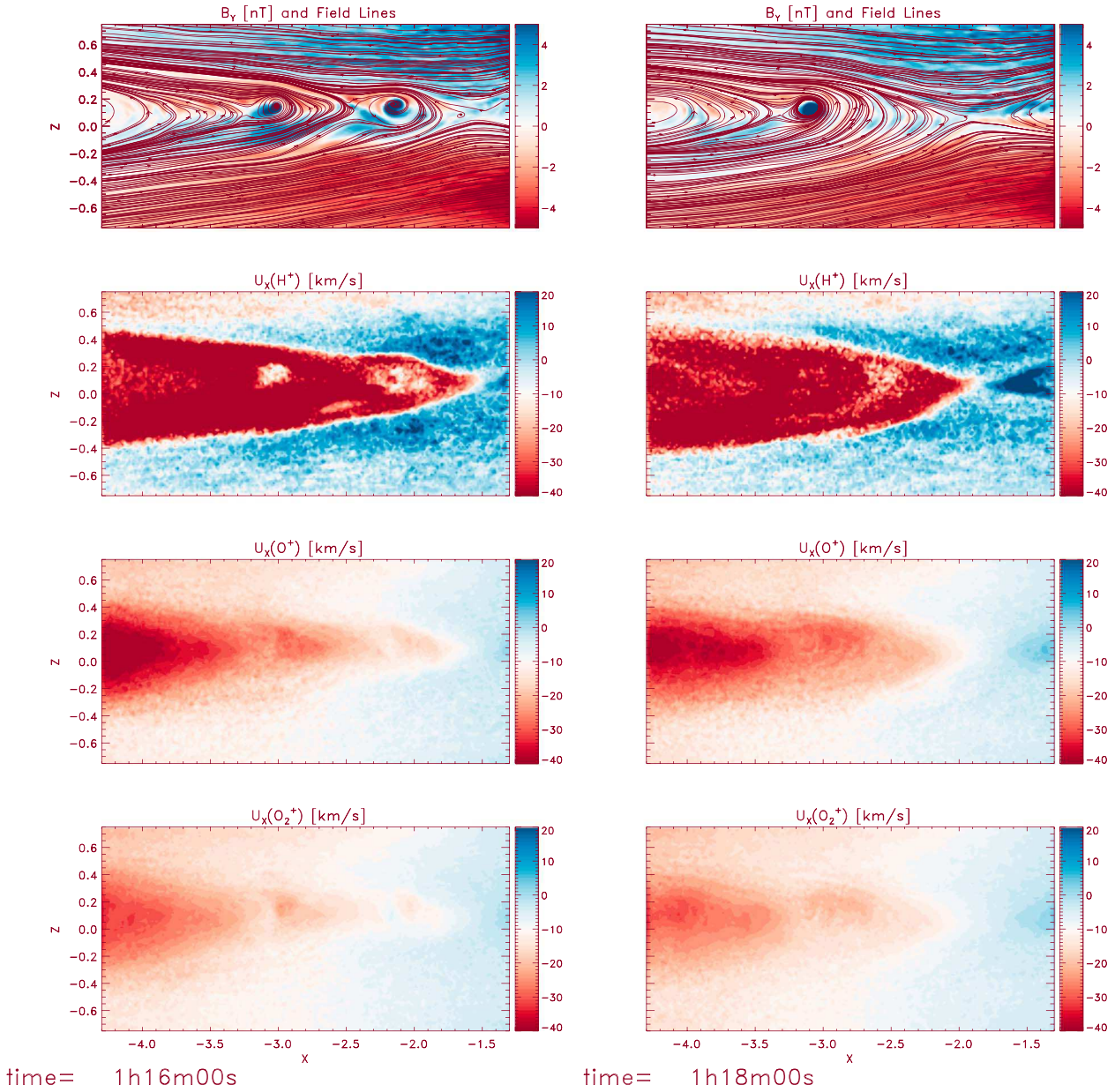

Figure 7. The out-of-plane magnetic field B_Y component with the in-plane magnetic field lines (top panels) and the X components of the flow velocities for three different ion species as calculated by the PIC model at time = 01:16 UT (left panels) and 01:18 UT (right panels).

time = 16 min and right panels are 2 min later, which are at the same time as the last two of Figure 6. The top panels show the out-of-plane magnetic field component B_Y with the in-plane magnetic field lines. The reconnection X point is roughly located at $-1.55R_M$ at 01:16 UT and moved to $-1.85R_M$ at 01:18 UT. The quadruple signature of the out-of-plane Hall magnetic component B_Y is clearly shown along the separatrix of the reconnection site. The panels below are U_X of H^+, O^+ and $O_2{}^+$ with positive values indicating Mars-ward flow, and negative values for tail-ward flow. The plasma flow patterns are similar for different ions with the plasma outside (inside) of the magnetic reconnection site being accelerated tail-ward (Mars-ward). However, the flow velocities are clearly different for different ion species. The light ions (H^+) were accelerated to high velocity, while the heavier ions are slower. The peak value of U_X is about 50 km/s for H^+, and 6 km/s for O^+ and 4 km/s for $O_2{}^+$. In addition, the PIC model also predicts that the light ions (H^+) have a larger tail-ward plasma flow. Comparison of the left and right panels show that even though the

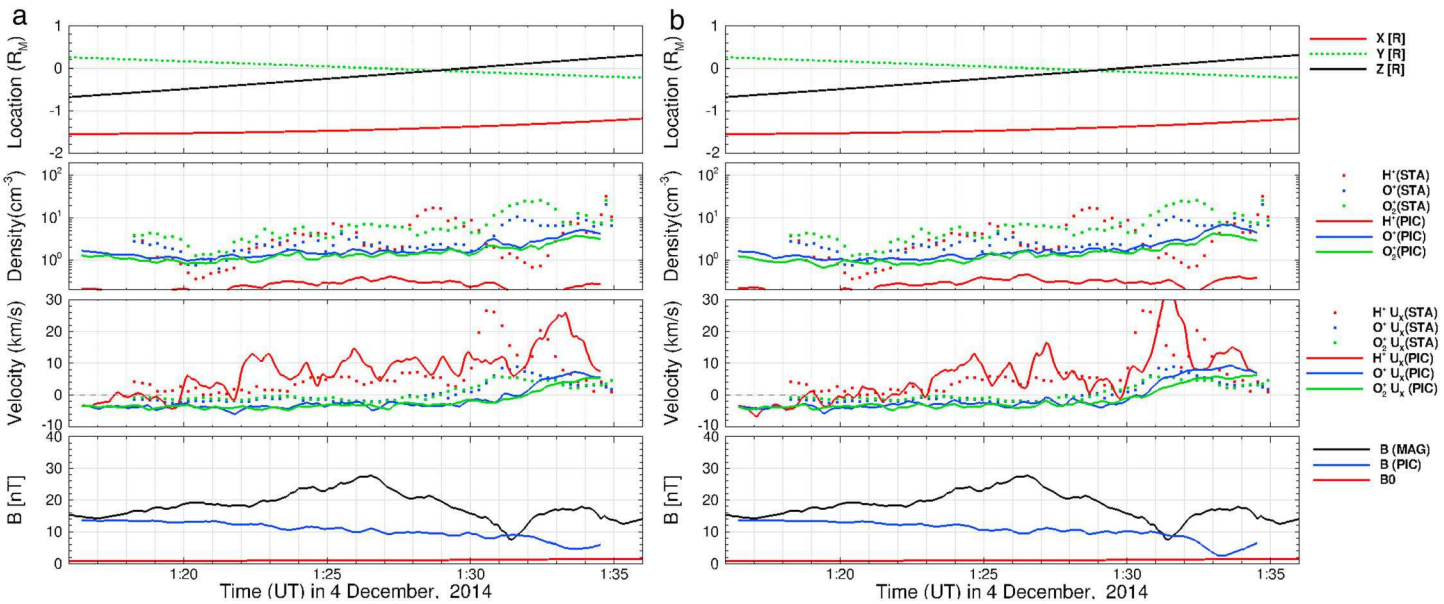

Figure 8. (a) Comparison of particle-in-cell (PIC) model results and plasma observations along Mars Atmosphere and Volatile EvolutioN orbit at time = 01:16 UT. Same format as Figure 4. (b) Same as Figure 8a at simulation time = 01:18 UT.

detailed structures are somewhat different at different simulation times, the general flow patterns remain similar.

Figures 8a and 8b show the extracted PIC model results along the MAVEN orbit at the same two times as in Figure 7. As can be seen from the second panel of Figure 8a, PIC model can reproduce the perturbations of plasma density to some extent but not as large as observed. Also PIC model results show lower ion densities compared with STATIC and HMHD (see Figure 4). This is likely due to the fact that ion source and loss terms are neglected in the PIC model. One important ion source in the Martian plasma tail is impact ionization. This process is included in the HMHD model but neglected in the PIC simulation. The third panel of Figure 8a shows velocity comparison along the MAVEN orbit. The model results follow the same trend as the observation for protons and two heavier planetary ions. The observed peak values of the three species are 26, 9, and 5.6 km/s, according to the STATIC measurements. The peak values from the model are consistent with observations. Model results at a later time as shown in Figure 8b are very similar to Figure 8a. The only notable difference is proton velocity, reaching more than 30 km/s. This clearly indicates the dynamic feature of the reconnection that was captured by the PIC model.

Figure 9 shows the magnetic field configuration in the tail region based on PIC simulation at 01:18 UT. The top panel shows a contour plot of the magnetic field strength in the *XZ* plane, with magnetic field lines in black. The central CS does not exactly lie in the equatorial plane but is shifted slightly northward, as indicated by the white horizontal line (Z = 0.06R_M). The bottom panel shows 3-D magnetic field lines and contour plots of magnetic field strength at four different *YZ* plane cuts to illustrate the 3-D structure of the current sheet. This clearly shows that the tail CS is not a straight plane, but is curved, especially away from the planet.

Figure 10 shows phase space velocity distributions at four selected locations based on PIC simulations at 01:18 UT. The four locations A–D are marked in Figure 9a by the purple boxes. The size of the boxes are $4\Delta x \times 16\Delta y \times 4\Delta z$, where $\Delta x,y,z$ are the grid resolution in the three orthogonal directions and equal to $1/64R_M$ (~50 km). Of the four locations, B is at the center of the reconnection site, while A and C are Mars-ward and tail-ward of the reconnection site, respectively. D is located inside the magnetic island tail-ward of the reconnection site. The distributions in both *Vx-Vy* (Figure 10a) and *Vy-Vz* (Figure 10b) space are shown for electrons, H^+ and O_2^+. The distributions of the three species at location B are most concentrated, indicating that plasma is relatively cold. All particles are thermalized away from the reconnection site, as the magnetic energy being partly converted to thermal energy. The gyrophase-bunched distributions are most notable for

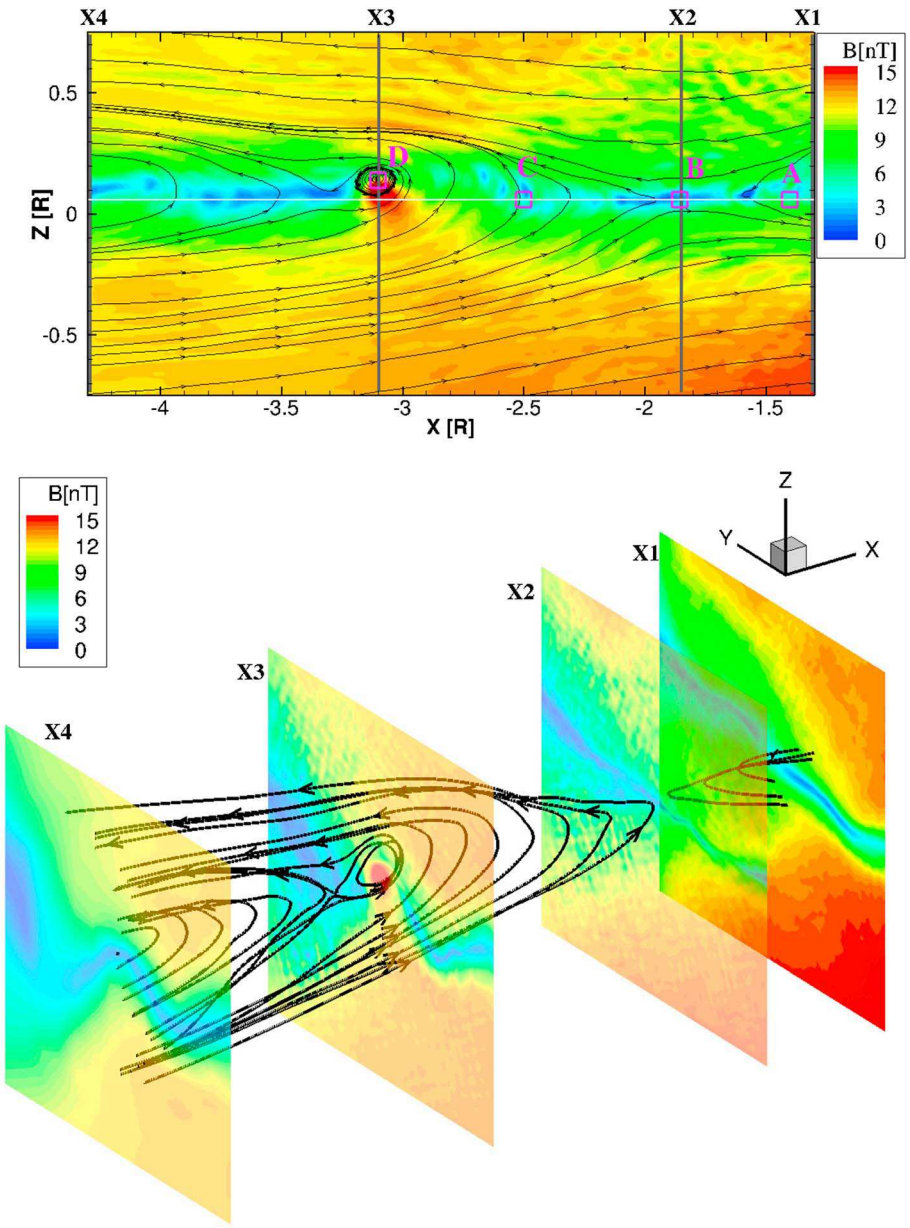

Figure 9. Tail magnetic field configuration based on particle-in-cell model results at 01:18UT. Top panel: Contour plot of the magnetic field strength in the *XZ* plane with magnetic field lines in black. The four vertical lines corresponding to $X_1 = -1.3R_M$, $X_2 = -1.85R_M$, $X_3 = -3.1R_M$, and $X_4 = -4.3R_M$. Bottom: 3-D view of the magnetic field lines and contour plots of magnetic field strength at corresponding *X* plane cuts.

H^+ and O_2^+ at location D in the perpendicular (*YZ*) velocity planes. Location D is inside the magnetic island, where the magnetic field is mainly in *X* direction (~15 nT). Such a phase space distribution is also present for O_2^+ ion in V_X-V_Y space at location C, where the magnetic field is mainly in *Z* direction. Gyrophase-bunched distributions was also detected in the immediate downstream of low Mach number shocks for heavy ions and can excite electromagnetic ion cyclotron waves (Lee & Lee, 2016; Lee & Wu, 2000).

Figure 11 shows plasma thermal pressure, magnetic pressure, and plasma beta in the *XZ* plane from PIC simulation at time = 01:18 UT. Plasma thermal pressure is relatively high in the CS where the magnetic pressure is weak. The plasma changes from low beta in the tail lobe to high beta plasma in the plasma sheet region. In the lobe region, the magnetic pressure is somewhat higher in the right lower corner due to relative strong crustal field in the region. The asymmetry in the crustal field distribution also causes asymmetric pressure (density) distribution in the two tail lobes near Mars.

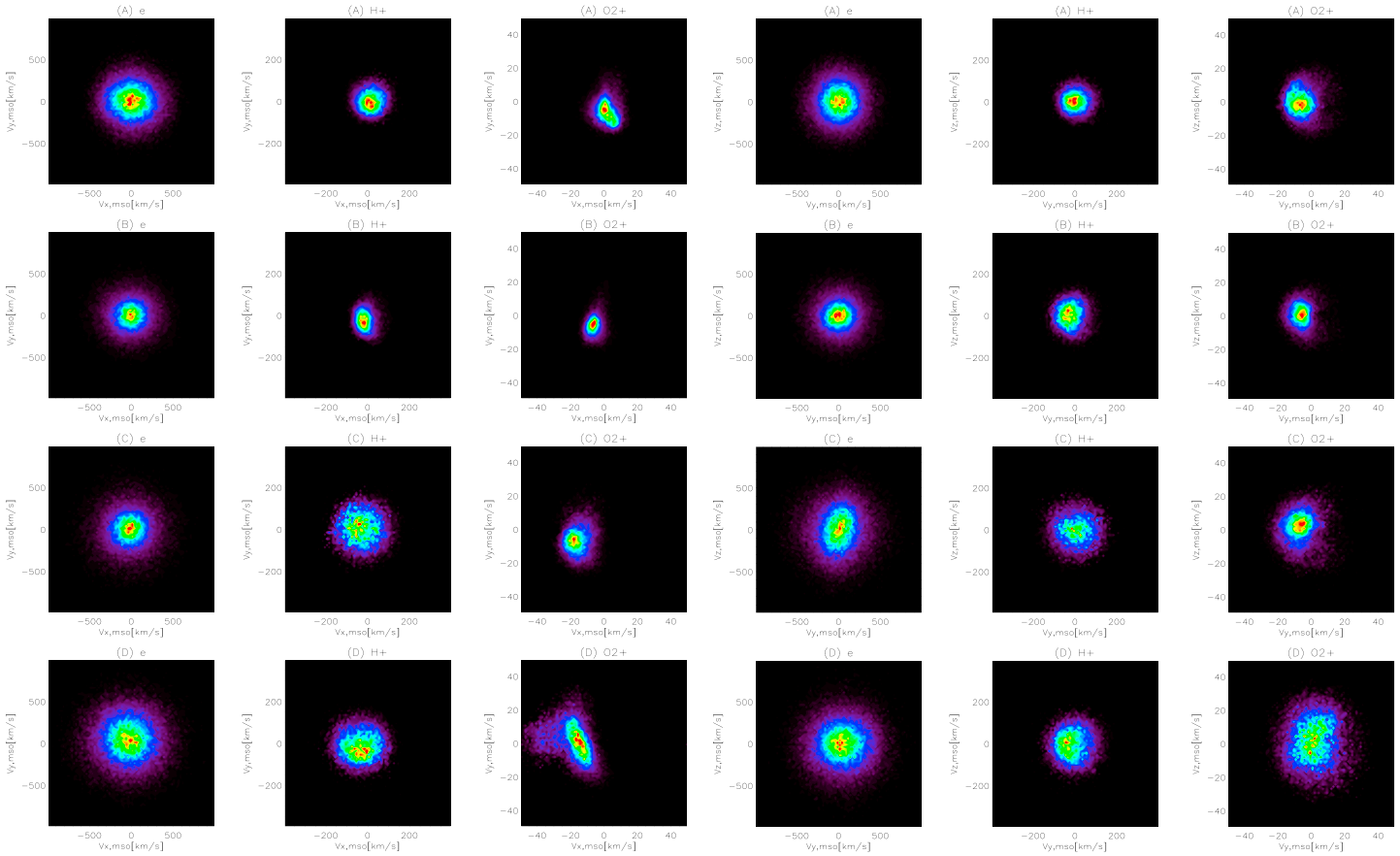

Figure 10. (a) Normalized phase space velocity distribution in V_X-V_Y space at four tail locations for three species (electron, H^+, and O_2^+) based on particle-in-cell results at 01:18 UT. The four locations are marked by the purple boxes in Figure 9a. The centers of these locations are A (−1.4, 0.06), B (−1.85, 0.0, 0.06), C (−2.5, 0.0, 0.06), and D (−3.1, 0.0, 0.14). The size of the boxes are $4\Delta x \times 16\Delta y \times 4\Delta z$, where $\Delta x,y,z$ are the grid resolution in the three orthogonal directions and equal to $1/64R_M$ (~50 km). Note that different velocity scales are used for different species. (b) Normalized phase space velocity distribution in V_Y-V_Z space at the same four tail locations for three species (electron, H^+, and O_2^+) at time = 01:18 UT.

Figure 12 shows various plasma parameters across the CS at $X = -1.85R_M$, as shown by the gray vertical line marked by X_2 in Figure 9a. The top panel shows that the tail plasma is dominated by O^+ and O_2^+. There is a clear enhancement of the ion densities inside the CS as compared with the lobe region. The plasma density near the right edge is high mainly due to transport from the dayside ionosphere. The asymmetric ion density distribution in the south-north (Z) direction is due to nonuniform distribution of the crustal magnetic field. The electron velocity is oscillating, mostly due to the fact that the electron scale is not very well resolved in the PIC simulation. Proton velocity reaches about 35 km/s in Y direction, while the velocities of heavy ions (O^+ and O_2^+) are less than 10 km/s. Even through the H^+ velocity is much higher than the heavy ions (O^+ and O_2^+), as shown by the second panel, the current is mainly carried by O^+ (as shown in the third panel), due to much larger densities of O^+. The fourth panel shows thermal pressure profiles of various components with the dominant one being the O^+ pressure. The last panel shows total plasma thermal pressure (sum of thermal pressure for all the components), magnetic pressure, and the ratio of the two (plasma beta). The plasma beta is about 0.02 in the southern lobe, 0.7 in the northern lobe, and reaches 60 in the center of the CS.

Figure 13 is a similar plot as Figure 12 but along the center of the CS at $z = -0.06R_M$ (as shown by the white horizontal line in Figure 9a). As shown in the top panel, the density peaks at around $1.8R_M$ near the reconnection site and gradually drops away from the site. Velocities of different components in the X direction are plotted in the second panel. As discussed before, the light ion (H^+) is accelerated to a much higher velocity than O^+ and O_2^+. To understand why the light ions are accelerated to a higher velocity in X direction away from the reconnection site, we examined the different forces along the direction. The main forces exerted

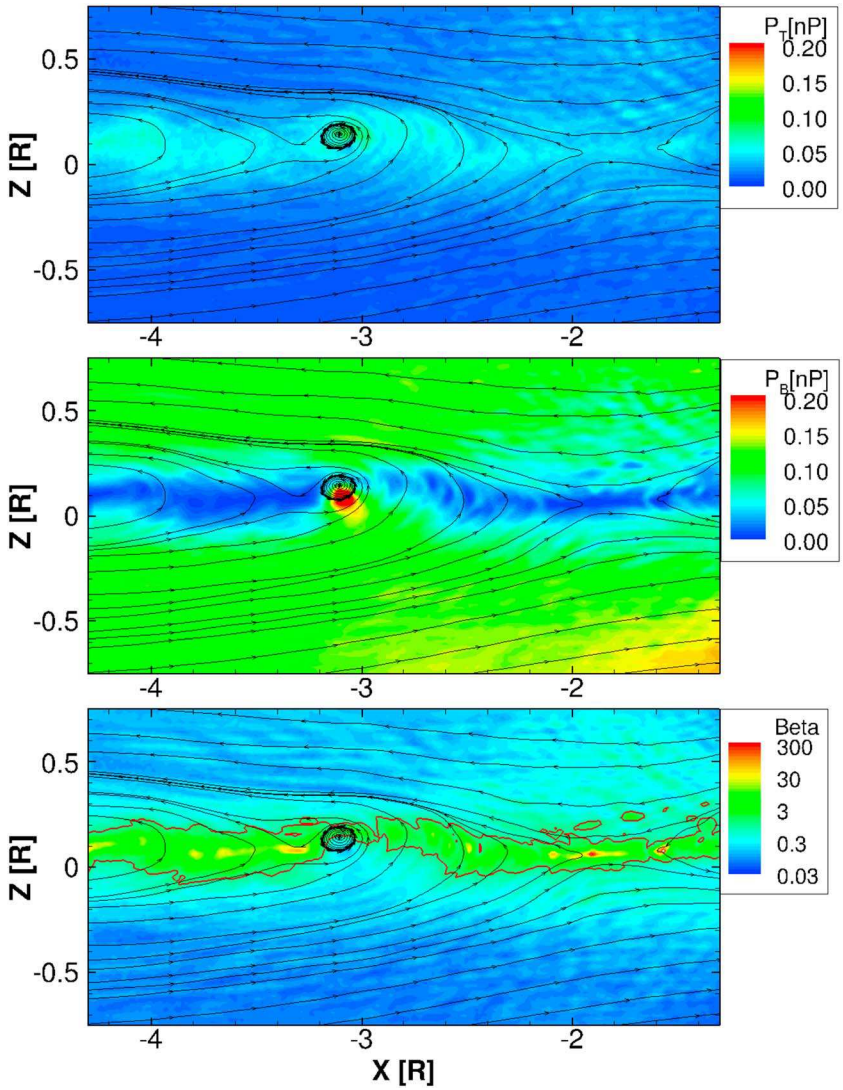

Figure 11. Contour plot of plasma thermal pressure, magnetic pressure, and plasma beta in the *XZ* plane from particle in cell at time = 01:18 UT. The black lines are magnetic field lines. Red lines in the bottom panel are contour line of plasma beta = 1.0.

on an ion particle are electric field force, $U \times B$ force and pressure gradient force. Thus, the total force that exerts on an ion particle can be expressed as

$$m_i \frac{d\boldsymbol{u}_i}{dt} = q_i \boldsymbol{E} + q_i (\boldsymbol{u}_i \times \boldsymbol{B}) - \frac{\nabla P_i}{n_i}$$

where $\boldsymbol{E} = -(\boldsymbol{u}_e \times \boldsymbol{B}) - \frac{\nabla P_e}{e n_e}$.

The pressure gradient forces are about 2 orders of smaller than the other forces in this direction and thus can be safely neglected. So the motions of ion particles depend on their charge over mass ratio (q_i/m_i) or simply mass since all the particles are single charged. The force along the *X* direction for the electric field ($F[E] = q_iE$) is plotted along the CS together with $U \times B$ forces $F(U \times B)$ for H^+, O^+, and O_2^+ (see bottom panel). The $U \times B$ forces are similar for O^+ and O_2^+ and comparable to electric field force. As a result, the acceleration of O^+ is about twice that of O_2^+, while the $U \times B$ force for H^+ is more complicated. Because H^+ is much lighter than O^+ and O_2^+, it is easily accelerated to a large velocity at a small distance from the reconnection site by the electric field force. This large velocity causes the light ions to gyrate around the magnetic field (see velocity phase distribution in *Vx-Vy* space at location C for H^+ in Figure 10a). The different ions reach roughly the same

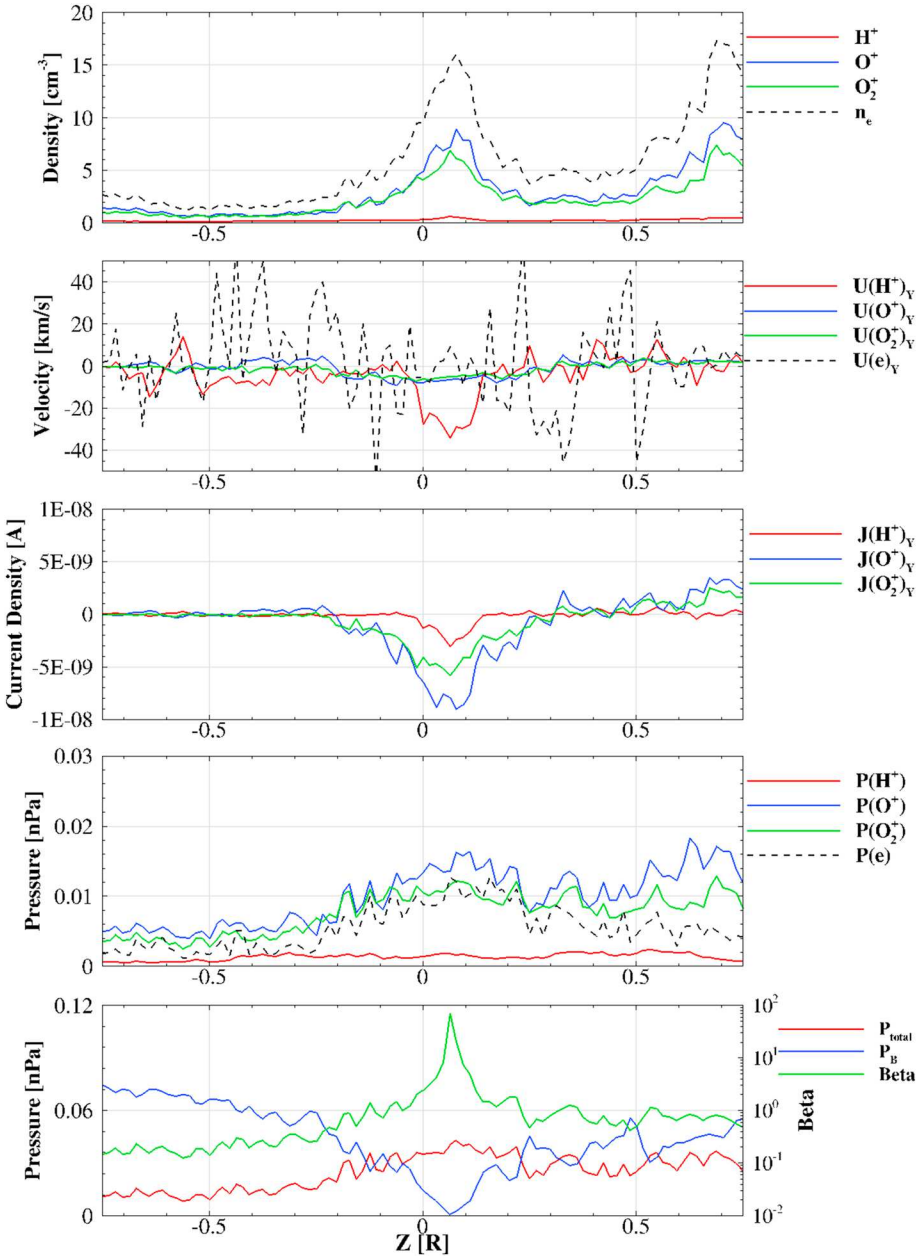

Figure 12. Plasma properties along a line cut in *Z* direction at $X = -1.85R_M$ in the *XZ* plane from the particle-in-cell simulation at time = 01:18 UT.

velocity beyond $3.5R_M$ from the tail region due to electromagnetic forces, which slow down the fast-moving ion particles and accelerate the slow-moving particles.

4.3. Escape Rates

The integrated ion escape rates are plotted in Figure 14a for both the time-dependent HMHD and HMHD EPIC model for a 20-min time period. Both models predict that O^+ is the dominant ion being lost to space, and the escape rates are fairly constant for the time period. The ratio of O^+ versus O_2^+ is about 1.35. The total escape rate increases from 8.8×10^{24} s^{-1} to 9.4×10^{24} s^{-1} for HMHD while it varies between 8.6×10^{24} s^{-1} to 9.2×10^{24} s^{-1} for HMHD EPIC model. Overall, the escape rates from the HMHD are similar to that of HMHD EPIC, except that the HMHD EPIC model predicts that the ion loss rates are more variable and appear to be quasiperiodic, likely due to the magnetic reconnection process and the associated tail-ward moving

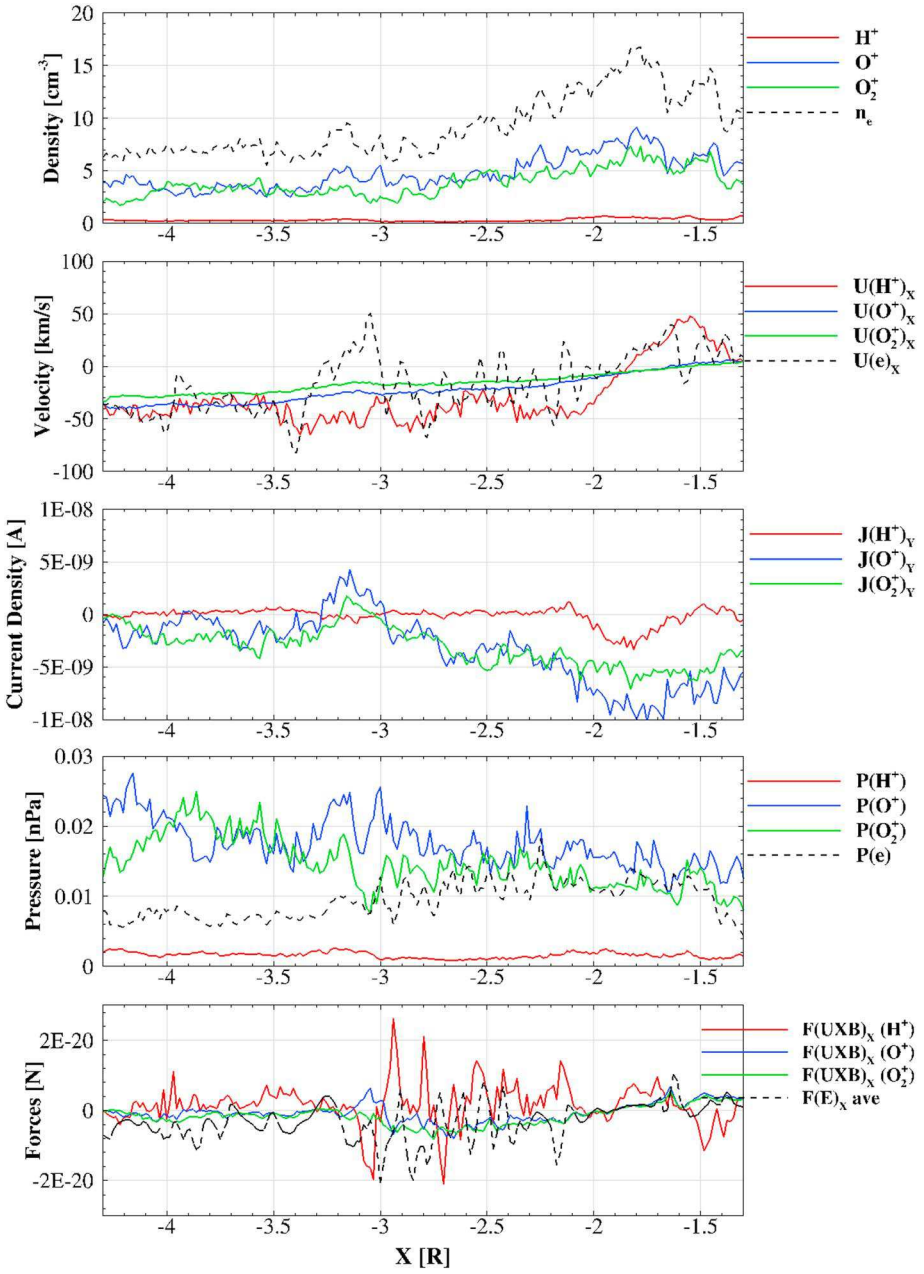

Figure 13. Plasma properties along a line cut at $Z = -0.06R_M$ in the *XZ* plane from the particle-in-cell simulation at time = 01:18 UT.

plasmoids. Such results are consistent with Geospace Environmental Modeling challenge results (Birn & Hesse, 2001), which concluded that all models that include the Hall effect in the generalized Ohm's law produce similar rates of reconnection, corresponding to nearly Alfvénic inflow velocities.

Also note that the ion loss rates are calculated based on output from the global HMHD model in both cases by integrating the fluxes passing through a spherical shell with a radius of $3R_M$. Even though the PIC simulation suggests that different ions have different velocities due to magnetic reconnection, these effects were smeared out in the single-fluid HMHD model. As a result, the calculated escape rates of light (heavy) ions are somewhat underestimated (overestimated), as illustrated in Figure 14b. This figure shows how many ions are lost through different *X* cuts of the PIC domain based on both PIC and HMHD results at 01:18 UT. The ion loss rate through the tail region (inside $|Y| < 0.75R_M$ and $|Z| < 0.75R_M$) is around 2.0×10^{24} s^{-1}, accounting for roughly 25% of the total ion loss rate. The tail loss rates vary significantly as a function of the distance to the

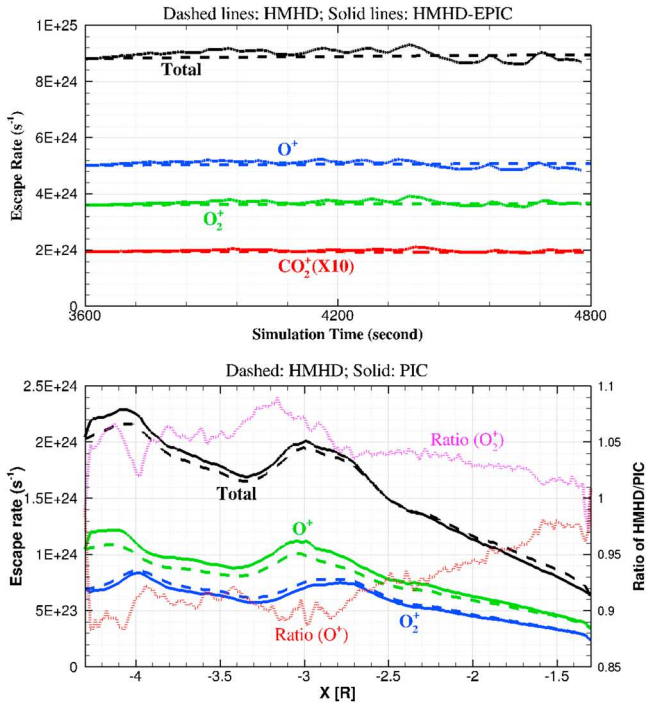

Figure 14. Top: Comparison of ion loss rates of the Hall-magnetohydrodynamic (HMHD) model (dashed lines) and HMHD with embeded particle-in-cell (solid lines). Bottom: Comparison of tail ion loss rates of the HMHD (dashed lines) model and particle-in-cell (PIC; solid lines). The ratio of HMHD/PIC for O^+ and O_2^+ are plotted in red and purple dotted lines, respectively.

planet. From $1.3R_M$ to $3R_M$, the escape rates increase by a factor of 3. Between $3R_M$ and $4R_M$, the escape rates first decrease and then increase due to the propagation of the plasmoids associated with magnetic islands. Figure 14b also shows the ratio of ion escape rates between the HMHD and PIC models to provide a quantitative view of the errors introduced in the escape rates calculation based on single-fluid assumption. Depending on location, O^+ escape rate can be underestimated by as much as 12%, while O_2^+ escape rate is overestimated up to 9% due to single-fluid assumption of the HMHD model. Considering the fact that the tail loss rate is about one fourth of the total ion loss rate, the error due to single-fluid assumption is negligible. The effects of the single-fluid assumption can also be seen at the boundary of PIC region (at $X = 1.3R_M$ and $4.3R_M$), where the ratio was forced to be 1.0 by the boundary condition.

5. Summary

Both the HMHD model and the HMHD EPIC model are used to study the magnetic reconnection event observed by MAVEN on 4 December 2014, reported by Harada et al. (2015). The general interaction pattern is well reproduced by the HMHD model, consistent with MAVEN observations. But the HMHD model could not reproduce the small structures observed in the Martian plasma tail. To overcome the limitation of the fluid model, the magnetic reconnection event is also simulated with a two-way coupled HMHD EPIC model. This is the first time that we were able to conduct a kinetic simulation of the reconnection process in a global simulation using realistic solar wind conditions. While the boundary conditions at each step are provided by the HMHD model, the solution inside the PIC domain is fully determined by the PIC calculation. Thus, the PIC simulation reproduces a tail magnetic reconnection scenario with close to realistic plasma conditions (density, velocity, and composition) and magnetic configurations.

The HMHD EPIC model clearly shows that the Martian magnetotail is highly dynamic with magnetic islands forming in the tail region and propagating away from the planet with plasmoid containing planetary ions. Such a feature is missing in the global MHD model, which is likely due to the fact that the grid resolution used in the global MHD simulations is much coarser than the grids in the EPIC simulations in the tail region. The HMHD EPIC model predicts that the Mars-ward plasma flow velocities due to magnetic reconnection are higher for the lighter ions, quantitatively consistent with MAVEN observations. The averaged ion loss rates from the HMHD model are similar to the coupled model, except that the HMHD EPIC model predicts that the ion loss rates are more variable in time. Even though the PIC simulation suggests that different ions have different velocities due to magnetic reconnection, the error due to single-fluid assumption is negligible when evaluating the total ion loss rate.

It is important to note that the electron-scale physics is not fully captured in the HMHD EPIC model due to limitations of the grid resolution. However, this should not impact the main conclusions of the paper, because we mainly focused on processes at MHD scales, and the detailed structures at electron spatial/timescales should have minimal influence. It is also worth noting that there are some unavoidable inconsistencies at the interface of the MHD and PIC domains due to the different underlying treatments of the system (fluid vs. kinetic). Some of the kinetic information is lost when information is transferred from the PIC model to the global HMHD model. While these are valid concerns, our extensive experience with the MHD EPIC model (Chen et al., 2017; Daldorff et al., 2014; Tóth et al., 2016, 2017) shows that the two models can properly work together and there are no significant numerical artifacts at the interface.

Even though the rotation of the crustal field is included in the simulation, it is hard to quantify the effect of magnetic reconnection based on model results. This is because (a) the crustal field in the tail region near the reconnection site is rather weak and (b) the simulation time is about 20 min, with a corresponding rotation angle of only 5°. In the future, we will examine whether or not magnetic reconnection is continuously

occurring in the Martian plasma tail by conducting a longer simulation. We also found that the H^+ density was too small in the tail compared to observed values. This is likely due to the fact that the ionization process is neglected in the PIC model. Including source terms into the PIC model will be addressed in future work. We also plan in the future to couple the multifluid MHD model with PIC to improve the global model and make the coupling process more consistent.

Acknowledgments
The work was supported by NASA Mars exploration Program and NSF INSPIRE grant PHY-1513379. Resources supporting this work were provided by the NASA High-End Computing (HEC) Program through the NASA Advanced Supercomputing (NAS) Division at Ames Research Center. MAVEN data are available in the Planetary Data System. Simulation results can be obtained at http://ssc.igpp.ucla.edu/AGUdata/2018_JGR_MHDEPIC_pubdata/.

References

Angelopoulos, V., McFadden, J. P., Larson, D., Carlson, C. W., Mende, S. B., Frey, H., et al. (2008). Tail reconnection triggering substorm onset. *Science*, *321*(5891), 931–935. https://doi.org/10.1126/science.1160495

Arkani-Hamed, J. (2001). A 50-degree spherical harmonic model of the magnetic field of Mars. *Journal of Geophysical Research*, *106*, 23,197–23,208. https://doi.org/10.1029/2000JE001365

Arkani-Hamed, J. (2002). An improved 50-degree spherical harmonic model of the magnetic field of Mars derived from both high-altitude and low-altitude data. *Journal of Geophysical Research*, *107*(E10), 5083. https://doi.org/10.1029/2001JE001835

Barabash, S., Fedorov, A., Lundin, R., & Sauvaud, J. A. (2007). Martian atmospheric erosion rates. *Science*, *315*(5811), 501–503. https://doi.org/10.1126/science.1134358

Barabash, S., Fedorov, A., Sauvaud, J. J., Lundin, R., Russell, C. T., Futaana, Y., et al. (2007). The loss of ions from Venus through the plasma wake. *Nature*, *450*(7170), 650–653. https://doi.org/10.1038/nature06434

Birn, J., & Hesse, M. (2001). Geospace Environment Modeling (GEM) magnetic reconnection challenge: Resistive tearing, anisotropic pressure, and Hall effects. *Journal of Geophysical Research*, *106*(A3), 3737–3750. https://doi.org/10.1029/1999JA001001

Brain, D. (2006). Mars global surveyor measurements of the Martian solar wind interaction. *Space Science Reviews*, *126*(1–4), 77–112. https://doi.org/10.1007/s11214-006-9122-x

Brain, D. A., Baker, A. H., Briggs, J., Eastwood, J. P., Halekas, J. S., & Phan, T.-D. (2010). Episodic detachment of Martian crustal magnetic fields leading to bulk atmospheric plasma escape. *Geophysical Research Letters*, *37*, L14108. https://doi.org/10.1029/2010GL043916

Burch, J. L., Moore, T. E., Torbert, R. B., & Giles, B. L. (2016). Magnetospheric multiscale overview and science objectives. *Space Science Reviews*, *199*(1-4), 5–21. https://doi.org/10.1007/s11214-015-0164-9

Chen, Y., Tóth, G., Cassak, P., Jia, X., Gombosi, T. I., Slavin, J. A., et al. (2017). Global three-dimensional simulation of Earth's dayside reconnection using a two-way coupled magnetohydrodynamics with embedded particle-in-cell model: Initial results. *Journal of Geophysical Research: Space Physics*, *122*, 10,318–10,335. https://doi.org/10.1002/2017JA024186

Connerney, J. E. P., Espley, J., Lawton, P., Murphy, S., Odom, J., Oliversen, R., & Sheppard, D. (2015). The MAVEN magnetic field investigation. *Space Science Reviews*, *195*(1-4), 257–291. https://doi.org/10.1007/s11214-015-0169-4

Daldorff, L. K. S., Toth, G., Gombosi, T. I., Lapenta, G., Amaya, J., Markidis, S., & Brackbill, J. U. (2014). Two-way coupling of a global Hall magnetohydrodynamics model with a local implicit particle-in-cell model. *Journal of Computational Physics*, *268*, 236–254. https://doi.org/10.1016/j.jcp.2014.03.009

Daughton, W., Scudder, J., & Karimabadi, H. (2006). Fully kinetic simulations of undriven magnetic reconnection with open boundary conditions. *Physics of Plasmas*, *13*(7), 072101. https://doi.org/10.1063/1.2218817

Dubinin, E., Fraenz, M., Fedorov, A., Lundin, R., Edberg, N., Duru, F., & Vaisberg, O. (2011). Ion energization and escape on Mars and Venus. *Space Science Reviews*, *162*(1-4), 173–211. https://doi.org/10.1007/s11214-011-9831-7

Dungey, J. W. (1961). Interplanetary magnetic field and the auroral zones. *Physical Review Letters*, *6*(2), 47–48. https://doi.org/10.1103/physrevlett.6.47

Eastwood, J. P., Brain, D. A., Halekas, J. S., Drake, J. F., Phan, T. D., Øieroset, M., et al. (2008). Evidence for collisionless magnetic reconnection at Mars. *Geophysical Research Letters*, *35*, L02106. https://doi.org/10.1029/2007GL032289

Eparvier, F., Chamberlin, P., Woods, T., & Thiemann, E. (2015). The solar extreme ultraviolet monitor for MAVEN. *Space Science Reviews*, *195*(1–4), 293–301. https://doi.org/10.1007/s11214-015-0195-2

Halekas, J. S., Brain, D. A., & Eastwood, J. P. (2011). Large-amplitude compressive "sawtooth" magnetic field oscillations in the Martian magnetosphere. *Journal of Geophysical Research*, *116*, A07222. https://doi.org/10.1029/2011JA016590

Halekas, J. S., Eastwood, J. P., Brain, D. A., Phan, T. D., Øieroset, M., & Lin, R. P. (2009). Situ observations of reconnection hall magnetic fields at Mars: Evidence for ion diffusion region encounters. *Journal of Geophysical Research*, *114*, A11204. https://doi.org/10.1029/2009JA014544

Halekas, J. S., Taylor, E. R., Dalton, G., Johnson, G., Curtis, D. W., McFadden, J. P., et al. (2015). The solar wind ion analyzer for MAVEN. *Space Science Reviews*, *195*(1-4), 125–151. https://doi.org/10.1007/s11214-013-0029-z

Harada, Y., Halekas, J. S., McFadden, J. P., Espley, J., DiBraccio, G. A., Mitchell, D. L., et al. (2017). Survey of magnetic reconnection signatures in the Martian magnetotail with MAVEN. *Journal of Geophysical Research: Space Physics*, *122*, 5114–5131. https://doi.org/10.1002/2017JA023952

Harada, Y., Halekas, J. S., McFadden, J. P., Mitchell, D. L., Mazelle, C., Connerney, J. E. P., et al. (2015). Magnetic reconnection in the near-Mars magnetotail: MAVEN observations. *Geophysical Research Letters*, *42*, 8838–8845. https://doi.org/10.1002/2015GL065004

Hesse, M., Birn, J., & Kuznetsova, M. (2001). Collisionless magnetic reconnection: Electron processes and transport modeling. *Journal of Geophysical Research*, *106*, 3721–3735. https://doi.org/10.1029/1999JA001002

Jakosky, B. M., Grebowsky, J. M., Luhmann, J. G., Connerney, J., Eparvier, F., Ergun, R., et al. (2015). MAVEN observations of the response of Mars to an interplanetary coronal mass ejection. *Science*, *350*(6261), aad0210. https://doi.org/10.1126/science.aad0210

Karimabadi, H., Roytershteyn, V., Mouikis, C. G., Kistler, L. M., & Daughton, W. (2011). Flushing effect in reconnection: Effects of minority species of oxygen ions. *Planetary and Space Science*, *59*(7), 526–536. https://doi.org/10.1016/j.pss.2010.07.014

Krymskii, A. M., Breus, T. K., Ness, N. F., Acuña, M. H., Connerney, J. E. P., Crider, D. H., et al. (2002). Structure of the magnetic field fluxes connected with crustal magnetization and topside ionosphere at Mars. *Journal of Geophysical Research*, *107*(A9), 1245. https://doi.org/10.1029/2001JA000239

Kuznetsova, M. M., Hesse, M., Rastaetter, L., & Gombosi, T. (2004). Intermittent reconnection, flux ropes and vortices generation at the dayside magnetopause, *Eos Trans. AGU*, 85(47), Fall Meet. Suppl., Abstract SM51C-0387.

Kuznetsova, M. M., Sibeck, D. G., Hesse, M., Wang, Y., Rastaetter, L., Toth, G., & Ridley, A. (2009). Cavities of weak magnetic field strength in the wake of FTEs: Results from global magnetospheric MHD simulations. *Geophysical Research Letters*, *36*, L10104. https://doi.org/10.1029/2009GL037489

Lee, K. H., & Lee, L. C. (2016). Generation of he^+ and O^+ EMIC waves by the bunch distribution of O^+ ions associated with fast magnetosonic shocks in the magnetosphere. *Geophysical Research Letters*, *43*, 9406–9414. https://doi.org/10.1002/2016GL070465

Lee, L. C., & Wu, B. H. (2000). Heating and acceleration of protons and minor ions by fast shocks in the solar corona. *The Astrophysical Journal*, *535*(2), 1014–1026. https://doi.org/10.1086/308879

Lin, J., & Forbes, T. G. (2000). Effects of reconnection on the coronal mass ejection process. *Journal of Geophysical Research*, *105*, 2375–2392. https://doi.org/10.1029/1999JA900477

Liu, Y. H., Mouikis, C. G., Kistler, L. M., Wang, S., Roytershteyn, V., & Karimabadi, H. (2015). The heavy ion diffusion region in magnetic reconnection in the Earth's magnetotail. *Journal of Geophysical Research: Space Physics*, *120*, 3535–3551. https://doi.org/10.1002/2015JA020982

Ma, Y., Nagy, A. F., Sokolov, I. V., & Hansen, K. C. (2004). Three-dimensional, multispecies, high spatial resolution MHD studies of the solar wind interaction with Mars. *Journal of Geophysical Research*, *109*, A07211. https://doi.org/10.1029/2003JA010367

Ma, Y., Nagy, A. F., Toth, G., Cravens, T. E., Russell, C. T., Gombosi, T. I., et al. (2007). 3D global multi-species Hall-MHD simulation of the Cassini T9 flyby. *Geophysical Research Letters*, *34*, L24S10. https://doi.org/10.1029/2007GL031627

Ma, Y. J., Fang, X., Russell, C. T., Nagy, A. F., Toth, G., et al. (2014). Effects of crustal field rotation on the solar wind plasma interaction with Mars. *Geophysical Research Letters*, *41*, 6563–6569. https://doi.org/10.1002/2014GL060785

Ma, Y. J., Russell, C. T., Fang, X., Dong, Y., Nagy, A. F., Toth, G., et al. (2015). MHD model results of solar wind interaction with Mars and comparison with MAVEN plasma observations. *Geophysical Research Letters*, *42*, 9113–9120. https://doi.org/10.1002/2015GL065218

Markidis, S., Henri, P., Lapenta, G., Divin, A., Goldman, M., Newman, D., & Laure, E. (2013). Kinetic simulations of plasmoid chain dynamics. *Physics Plasmas*, *20*(8), 082105. https://doi.org/10.1063/1.4817286

Markidis, S., Lapenta, G., Bettarini, L., Goldman, M., Newman, D., & Andersson, L. (2011). Kinetic simulations of magnetic reconnection in presence of a background O+ population. *Journal of Geophysical Research*, *116*, A00K16. https://doi.org/10.1029/2011JA016429

Markidis, S., Lapenta, G., & Uddin, R. (2010). Multi-scale simulations of plasma with iPIC3D. *Mathematics and Computers in Simulation*, *80*, 1509–1519. https://doi.org/10.1016/j.matcom.2009.08.038

Masuda, S., Kosugi, T., Hara, H., Tsuneta, S., & Ogawara, Y. (1994). A loop-top hard X-ray source in a compact solar flare as evidence for magnetic reconnection. *Nature*, *371*, 495–497.

McFadden, J. P., Kortmann, O., Curtis, D., Dalton, G., Johnson, G., Abiad, R., et al. (2015). The MAVEN Suprathermal and Thermal Ion Composition (STATIC) instrument. *Space Science Reviews*, *195*(1–4), 199–256. https://doi.org/10.1007/s11214-015-0175-6

Morschhauser, A., Lesur, V., & Grott, M. (2014). A spherical harmonic model of the lithospheric magnetic field of Mars. *Journal of Geophysical Research, Planets*, *119*, 1162–1188. https://doi.org/10.1002/2013JE004555

Mozer, F. S., Bale, S. D., & Phan, T. D. (2002). Evidence of diffusion regions at a sub-solar magnetopause crossing. *Physical Review Letters*, *89*(1), 015002. https://doi.org/10.1103/PhysRevLett.89.015002

Nagy, A. F., Winterhalter, D., Sauer, K., Cravens, T. E., Brecht, S., Mazelle, C., et al. (2004). The plasma environment of Mars. *Space Science Reviews*, *111*(1/2), 33–114. https://doi.org/10.1023/B:SPAC.0000032718.47512.92

Øieroset, M., Phan, T. D., Fujimoto, M., Lin, R. P., & Lepping, R. P. (2001). In situ detection of collisionless reconnection in the Earth's magnetotail. *Nature*, *412*(6845), 414–417. https://doi.org/10.1038/35086520

Paschmann, G., Øieroset, M., & Phan, T. (2013). In-situ observations of reconnection in space. *Space Science Reviews*, *178*(2–4), 385–417. https://doi.org/10.1007/s11214-012-9957-2

Paschmann, G., Sonnerup, B. U. Ö., Papamastorakis, I., Sckopke, N., Haerendel, G., Bame, S. J., et al. (1979). Plasma acceleration at the earth's magnetopause: Evidence for reconnection. *Nature*, *282*(5736), 243–246. https://doi.org/10.1038/282243a0

Peng, I. B., Markidis, S., Vaivads, A., Vencels, J., Amaya, J., Divin, A., et al. (2015). The formation of a magnetosphere with implicit particle-in-cell simulations. *Procedia Computer Science*, *51*, 1178–1187.

Phan, T. D., Kistler, L. M., Klecker, B., Haerendel, G., Paschmann, G., Sonnerup, B. U. Ö., et al. (2000). Extended magnetic reconnection at the Earth's magnetopause from detection of bi-directional jets. *Nature*, *404*(6780), 848–850. https://doi.org/10.1038/35009050

Powell, K. G., Roe, P. L., Linde, T. J., Gombosi, T. I., & DeZeeuw, D. L. (1999). A solution-adaptive upwind scheme for ideal magnetohydrodynamics. *Journal of Computational Physics*, *154*(2), 284–309. https://doi.org/10.1006/jcph.1999.6299

Raeder, J. (2006). Flux transfer events: 1. Generation mechanism for strong southward IMF. *Annales de Geophysique*, *24*(1), 381–392. https://doi.org/10.5194/angeo-24-381-2006

Russell, C. T. (2001). The dynamics of planetary magnetospheres. *Planetary and Space Science*, *49*(10-11), 1005–1030. https://doi.org/10.1016/S0032-0633(01)00017-4

Russell, C. T., Luhmann, J. G., Cravens, T. E., Nagy, A. F., & Strangeway, R. J. (2007). Venus upper atmosphere and plasma environment: Critical issues for future exploration. In *Exploring Venus as a terrestrial planet*, *Geophys. Monograph Series* (Vol. 175, pp. 139–156). Washington DC: AGU. https://doi.org/10.1029/176GM09

Russell, C. T., Luhmann, J. G., & Strangeway, R. J. (2006). The solar wind interaction with Venus through the eyes of the Pioneer Venus Orbiter. *Planetary and Space Science*, *54*(54), 1482–1495. https://doi.org/10.1016/j.pss.2006.04.025

Russell, C. T., Saunders, M. A., Phillips, J. L., & Fedder, J. A. (1986). Near-tail reconnection as the cause of cometary tail disconnections. *Journal of Geophysical Research*, *91*, 1417–1423. https://doi.org/10.1029/JA091iA02p01417

Schunk, R. W., & Nagy, A. F. (2009). *Ionospheres*, (2nd ed.). New York: Cambridge University Press. https://doi.org/10.1017/CBO9780511635342

Schwingenschuh, K., Riedler, W., Zhang, T.-L., Lichtenegger, H., Rosenbauer, H., Livi, S., et al. (1992). The Martian magnetic field environment: Induced or dominated by an intrinsic magnetic field? *Advances in Space Research*, *129*, 9213.

Sonnerup, B. U. Ö. (1979). Magnetic field reconnection. In L. J. Lanzerotti, C. F. Kennel, & E. N. Parker (Eds.), *Solar system plasma physics* (Vol. III, pp. 45–108). Amsterdam: North-Holland.

Southwood, D. J., & Chané, E. (2016). High-latitude circulation in giant planet magnetospheres. *Journal of Geophysical Research: Space Physics*, *121*, 5394–5403. https://doi.org/10.1002/2015JA022310

Tóth, G., Chen, Y., Gombosi, T. I., Cassak, P., Markidis, S., & Peng, B. (2017). Scaling the ion inertial length and its implications for modeling reconnection in global simulations. *Journal of Geophysical Research: Space Physics*, *122*, 10,336–10,355. https://doi.org/10.1002/2017JA024189

Tóth, G., Jia, X., Markidis, S., Peng, I. B., Chen, Y., Daldorff, L. K. S., et al. (2016). Extended magnetohydrodynamics with embedded particle-in-cell simulation of Ganymede's magnetosphere. *Journal of Geophysical Research: Space Physics*, *121*, 1273–1293. https://doi.org/10.1002/2015JA021997

Tóth, G., van der Holst, B., Sokolov, I. V., de Zeeuw, D. L., Gombosi, T. I., Fang, F., et al. (2012). Adaptive numerical algorithms in space weather modeling. *Journal of Computational Physics*, *231*(3), 870–903. https://doi.org/10.1016/j.jcp.2011.02.006

Vignes, D., Mazelle, C., Rme, H., Acuña, M. H., Connerney, J. E. P., Lin, R. P., et al. (2000). The solar wind interaction with Mars: Locations and shapes of the bow shock and magnetic pile-up boundary from the observations of the MAG/ER experiment onboard Mars Global Surveyor. *Geophysical Research Letters*, *27*, 49–52.

Yamada, M., Kulsrud, R., & Ji, H. (2010). Magnetic reconnection. *Reviews of Modern Physics*, *82*(1), 603–664. https://doi.org/10.1103/RevModPhys.82.603

Yeroshenko, Y., Riedler, W., Schwingenschuh, K., Luhmann, J. G., Ong, M., & Russell, C. T. (1990). The magnetotail of Mars: Phobos observations. *Geophysical Research Letters*, *17*, 885–888.

Yokoyama, T., Akita, K., Morimoto, T., Inoue, K., & Newmark, J. (2001). Clear evidence of reconnection inflow of a solar flare. *The Astrophysical Journal*, *546*(1), L69–L72. https://doi.org/10.1086/318053

Zhang, T. L., Lu, Q. M., Baumjohann, W., Russell, C. T., Fedorov, A., Barabash, S., et al. (2012). Magnetic reconnection in the near Venusian magnetotail. *Science*, *336*(6081), 567–570. https://doi.org/10.1126/science.1217013